THESIS FOR THE DEGREE OF LICENTIATE OF ENGINEERING

# Passive Island Detection of Microgrid by Grid Forming Inverter

Shoaib Inamdar

Department of Electrical Engineering
Chalmers University of Technology
Gothenburg, Sweden, 2022

**Passive Island Detection of Microgrid by Grid Forming Inverter**

Shoaib Inamdar



Technical Report No. 1111-111X
ISSN 3.1415-9265
This thesis has been prepared using LaTeX.

Department of Electrical Engineering
Chalmers University of Technology
SE-412 96 Gothenburg, Sweden
Phone: +46 (0)31 772 1000
`www.chalmers.se`

Printed by Chalmers Reproservice
Gothenburg, Sweden, November2022

*To the Almighty and my family.*

**Passive Island Detection of Microgrid by Grid Forming Inverter**

SHOAIB INAMDAR
Division of Electrical Power Engineering
Department of Electrical Engineering
Chalmers University of Technology

# Abstract

The supply reliability of a local grid will be improved if the local grid is managed as a microgrid, with the ability to operate in island mode when the main grid is temporarily unavailable. This thesis focuses on microgrids powered by inverter-based resources (IBRs), one or several of which need to be equipped with grid forming (GFM) capability for establishing and controlling the voltage and frequency of the microgrid during island operation. To achieve a stable island operation, the detection of an islanding event is crucial.

The main aim of the thesis is to investigate how the different parameters of a virtual synchronous machine (VSM)-based GFM controller affect the performance of the existing passive island detection methods (IDMs). The analyses have been carried out using a medium-voltage microgrid with IBRs through theoretical evaluations, simulation studies, and laboratory verification. It is found that to achieve a small non-detection zone (NDZ) for a voltage vector shift (VVS) based passive IDM, a relatively large virtual reactance is desired. In contrast, a large virtual reactance may increase the risk of misdetection during a load switching event. However, a larger value of virtual reactance is preferred during the grid-connected condition to mitigate the impact of grid impedance estimation error on the design of the voltage controller. Furthermore, a fast synchronization loop, corresponding to a low value of virtual inertia constant and damping in the VSM structure, reduces not only the island detection time but also the risk of misdetection when facing a large variation in the grid frequency or angle jump in the grid voltage. Therefore, when tuning the VSM control parameters, it is necessary to weigh the importance of the need for inertia support and damping during grid-connected conditions and the need for a reliable and fast island detection method. Moreover, an analytical expression has also been derived on the relation between the island detection time and the virtual inertial constant and damping con-

stant. The relation is further verified in a laboratory experiment. This makes it convenient to tune the virtual inertial constant and damping constant of the VSM controller for a given required island detection time without resorting to time domain simulation. Besides the foregoing analyses, this thesis has also proposed a PQ-based method for estimating the cycle-to-cycle load angle jump for the VVS-based IDM. The method has shown better accuracy than the typical dq-based method as the PQ-based method is less sensitive to the electrical transients within each electrical cycle and less affected by the harmonics in the grid.

**Keywords:** Grid forming, inertia, microgrid, non-detection zone, passive island detection, rotor angle deviation, virtual synchronous machine, voltage vector shift.

# Acknowledgment

Words cannot express my gratitude to my supervisors Dr. Peiyuan Chen and Dr. Ritwik Majumder as well as to my examiner Prof. Dr. Massimo Bongiorno for their invaluable guidance, patience, and feedback. I also could not have undertaken this journey without the generous financial support from the Swedish Energy Agency under the SamspEL program.

I thank my brilliant office-mates David and Junfei for the fun banter we had together. I also raise my warmest gratitude to all the colleagues at Electrical Power Engineering who were available to answer my queries. I would be remiss in not mentioning my dear friend Anant for having the technical brainstorming sessions at times and supporting me with suggestions when required.

I am grateful to my family, especially my parents and my brother Saeed to whom I am deeply indebted for their love and support. Had it not been for their understanding and belief in me, this endeavor would not have been possible.

Last but certainly not least, I would like to thank my wife Sana for her love and understanding, especially during all the busy hours I had. It is her from whom I learned to enjoy little things and enjoy life to the fullest.

Shoaib Inamdar
Gothenberg, November 2022

# List of abbreviations

The following is the list of abbreviations in alphabetical order used in the thesis:

| | |
|---|---|
| BESS: | Battery Energy Storage System |
| DER: | Distributed Energy Resource |
| DFT: | Discrete Fourier Transform |
| EMF: | Electro-Motive Force |
| GFL: | Grid Following |
| GFM: | Grid Forming |
| IBR: | Inverter-based Resources |
| IDM: | Island Detection Method |
| LPF: | Low Pass Filter |
| MG: | Microgrid |
| NDZ: | Non-Detection Zone |
| NMG: | Nested Microgrid |
| PCC: | Point of Common Coupling |
| PI: | Proportional-Integral |
| PSC: | Power Synchronization Control |
| PV: | Photovoltaic |
| RES: | Renewable Energy Source |
| RoCoF: | Rate of Change of Frequency |

| | |
|---|---|
| VCC: | Vector Current Control |
| VSC: | Voltage Source Converter |
| VSM: | Virtual Synchronous Machine |
| VVS: | Voltage Vector Shift |

# Contents

# CHAPTER 1

# Introduction

## 1.1 Background and motivation

European Union (EU) countries aim to reduce $CO_2$ emissions significantly and be climate neutral by 2050 to limit the global temperature rise according to the Paris agreement[1]. However, the latest United Nations Intergovernmental Panel on Climate Change (IPCC) report shows that it will be almost impossible to limit the temperature rise to 1.5° if the $CO_2$ emissions are not reduced by 43% before 2030 [2]. This has led to an acceleration of the generation technology shift in the electricity section from the traditional fossil fuel powered thermal generators to the renewable energy source (RES)-based generators, such as wind, solar PV, hydro power, and bio-energy. In EU, it is predicted that the total share of electrical power from renewables will increase to 70% by 2030 with the aim of reducing the green house gas emissions by 55% in the same year [3]. Furthermore, in Sweden, the government has set a goal of 100% RESs-based electrical energy production by 2040 [4].

The integration of RESs into the power grid occurs at both the transmission system level and the distribution system level. At the local distribution system level, many countries, such as US, Greece, and Japan, have developed the so-called microgrids to facilitate the local integration of RESs at as low integration cost as possible. The U.S. Department of Energy defines the microgrid (MG) [5] as "a group of interconnected loads and distributed energy resources within clearly defined electrical boundaries that acts as a single controllable entity concerning the grid. An MG can connect and disconnect from the grid to enable it to operate in both grid-connected or island-mode." The main benefits of MG include:

- Increasing RES integration and contributing to clean energy goals;
- Reliable and resilient power supply to the customers in case of a grid failure or natural calamities;
- Reduction in transmission and distribution losses due to local electricity supply of demand;
- Mitigation of local grid capacity limitation caused by demand growth in the future;
- Supply of voltage and frequency ancillary services to the main grid by utilizing the available local generation.

On the other hand, there are also a number of challenges associated with MG operation, including

- Power balancing issues due to variable generation by renewable sources such as wind and solar;
- Complex multi-layer control structure to control various aspects within an MG to maintain normal operation as well as stability in case of maloperation;
- Requirement of a reliable protection system to identify and isolate faults in grid-connected and islanded mode of operation;
- Fast and accurate detection of an unintentional island to maintain the continuity of the electric supply to the customers;
- Regulatory framework to achieve a fair distribution of the monetary benefits obtained by utilities and/or MG owners to all the actors in the microgrid [6];

- High cost of the initial investment required for the deployment of MGs especially with sufficient storage systems and in the absence of regulations.

The benefits of individual MGs further motivate the interconnection of adjacent MGs to be operated as a single entity, which are referred to Nested Microgrids (NMGs). By sharing generation and energy storage resources between individual MGs, NMG aims to enhance its reliability and capability to support the main grid. The readers are referred to [7] for a more detailed discussion on benefits and challenges of NMGs.

In Sweden, there are limited pilot MG projects such as the Simris microgrid by E.ON and the Arholma microgrid by Vattenfall [8], [9]. However, there exists a number of drivers, as well as barriers, for the further development of MGs in Sweden [10]. In particular, the Swedish Electricity Act (1997:857) states that the grid operator should ensure that the electricity outage to an electricity consumer should never exceed 24 h [11]. Traditionally, to ensure supply availability and reliability, the grid operators build parallel overhead transmission lines or bury down underground cables. Erection of parallel transmission lines takes a long lead time whereas burying down underground cables are too costly, especially in low population density areas. An alternative approach to improve supply reliability and availability with a short implementation time is to enable the island operating capability of a distribution grid, as a key functionality of a so-called MG operation. This typically requires a battery energy storage system (BESS) to keep the power balance of the MG powered by intermittent renewables during island operation. Even though the cost of investing in a BESS is relatively high compared to a medium voltage cable, the investment of the BESS can still be justified if the BESS participates in providing flexibility and ancillary services to the main grid during grid-connected conditions.

In case of an unplanned interruption of electricity supply from the main grid, it is of great importance for the MG to detect such an outage in a fast and reliable way in order to transition to island operation smoothly. If the island condition fails to be detected in an MG with inverter-based resources (IBRs), the overcurrent protection setting keeps a relatively high fault current threshold as that for the grid-connected operation. In this case, a fault in the islanded MG may not be detected or isolated as the IBRs limit the fault current to the rated values of the inverters[12]. Consequently, the IBRs and/or the load may trip due to sustained undervoltage in the local grid and eventually lead to a local blackout. On the other hand, if a grid disturbance is mis-detected as an island, local loads may be unnecessarily disconnected. Thus, it is of great importance to have a fast and reliable island detection strategy for a successful MG operation.

## 1.2 Literature review on island detection methods for grid-forming inverters

Recently, the grid-forming (GFM) control of IBRs has been extensively discussed. However, the performance of the existing island detection methods (IDMs) for MGs powered by IBRs with GFM control has not been sufficiently explored. IDMs typically include communication-based, active IDMs, and passive IDMs [13]. These methods are commonly compared based on indices such as non-detection zone (NDZ) and island detection time ($T_{\mathrm{det}}$) [14], [15]. Communication-based IDM uses the breaker status signal at the substation [16] and hence has zero NDZ and a very short detection time. However, it is recommended not to rely solely on the breaker status signal and thus a backup IDM is required [17]. The active IDMs are based on real-time perturbation of electrical quantities, e.g. by applying a small change in the reactive power setpoint continuously [18]. The perturbation usually deteriorates the grid voltage quality, especially with multiple DERs [19]–[21]. To avoid actively disturbing the grid, passive IDMs are commonly used as a backup. Passive IDMs are simple to implement but suffer from a relatively large NDZ [22]. To reduce the NDZ, different composite IDMs are proposed to combine the voltage vector shift (VVS)-based and frequency-based IDMs [23]–[26]. The focus of this thesis is on the evaluation of passive IDMs as a backup in case of communication failure.

Passive IDMs are well studied for synchronous generators (SGs) [27]–[30] and for IBRs with grid-following (GFL) control [31]–[33] both in the context of anti-islanding protection and for MG island operation. In the latter case, selected IBRs with GFL control need to switch to GFM control once the islanded is detected. The island detection time is thus critical to prevent unstable operation of the IBRs with GFL control under island conditions. In contrast, if the IBRs are already equipped with GFM control during grid-connected conditions, the island detection time is no longer that critical as the IBRs with GFM control can form the voltage and frequency of the MG without the main grid [34]–[39]. On the other hand, if the island condition is left undetected, the MG becomes vulnerable when an additional fault occurs in the MG due to improper protection settings. This may cause cascaded generator and load tripping, which leads to a local blackout. Furthermore, there is usually a requirement on the maximum island detection time, e.g. the IEEE 1547 standard recommends 2 s as the maximum island detection time [40]. Moreover, in the future, GFM inverters may be controlled to provide different inertial support and damping control to the grid at different operating hours of a day depending on the reserve market price and grid conditions such as grid inertia and short-circuit strength [37], [38]. This will change the controller parameters of GFM inverters, which may affect the NDZ and island detection time of the passive IDMs [39]. To the best of the authors' knowledge, how the GFM control of IBRs affects the effectiveness of the passive IDMs has not been well studied in the existing literature.

## 1.3 Research questions

This thesis is going to address the following research questions:

1. Do the following two objectives impose a conflicting requirement on the tuning of a GFM controller?
    - performance requirement on the island detection of MG,
    - the need to provide grid ancillary services during the grid-connected mode.
2. What parameters of the GFM controller affect the NDZ and island detection time of an MG during an islanding event?
3. What controller parameters affect the risk of misdetecting grid disturbances as an islanding event?

## 1.4 Purpose of the thesis and main contributions

The main purpose of the thesis is to evaluate the performance of passive IDMs in an MG powered by IBR with the Virtual synchronous machine (VSM)-based GFM control. In particular, the thesis aims to identify limitations on the parameter tuning of the VSM-based GFM controller imposed by the performance requirement for island detection.

The main contributions of the thesis include:

1. Identification and evaluation of key VSM-based GFM controller parameters that affect the NDZ for VVS-based IDM

2. Determination and verification of the analytical expression of island detection time as a function of virtual inertia and damping provided by an inverter with VSM-based GFM control using frequency-based IDM. Such an analytical expression can be used to determine the maximum value of virtual inertia constant and damping given a desired detection time without resorting to time-domain simulations.

3. Evaluation of the risk of misdetecting various grid disturbances as an islanding event by an inverter with VSM-based GFM control using VVS-based and/or frequency-based IDM. This will provide recommendations on the trade-off between parameter selection for the VSM-based GFM controller design to successfully perform grid connected services and stable island operation.

4. Proposing a PQ-based load angle estimation for VVS-based IDM in case of MGs powered by IBRs.

## 1.5 Thesis outline

The rest of the thesis chapters are organized as:

- Chapter 2 presents the overview of basic passive IDMs and GFM controllers implemented in the MG.

- Chapter 3 propose a PQ-based load angle estimation technique for VVS-based island detection. Furthermore, the chapter derives the relation between the VSM-based GFM controller parameters and the IDM performance indices such as NDZ and island detection time.

- Chapter 4 describes the case study system and simulation results analyzing the impact of VSM-based GFM controller on VVS- and frequency-based passive IDMs. The chapter also presents the cases with the possible risk of misdetection of grid disturbance as an island by the passive IDM.

- Chapter 5 apply the passive IDM in an experimental MG setup having VSM-based GFM control and verify the observations from simulation results.
- Chapter 6 summarize the conclusions and provide suggestions for future work.

## 1.6 List of publications

- S. Inamdar, R. Mohanty, P. Chen, R. Majumder and M. Bongiorno, "On Benefits and Challenges of Nested Microgrids," *2019 IEEE PES Asia-Pacific Power and Energy Engineering Conference (APPEEC), 2019*, pp. 1-6, doi: 10.1109/APPEEC45492.2019.8994363.
- S. Inamdar, P. Chen, R. Majumder, M. Bongiorno, "Impact of Grid Forming Control on the Effectiveness of Passive Island Detection," to be submitted to *IEEE Transactions on Smartgrid* (Submitted)

# CHAPTER 2

## Overview of Backup Passive Island Detection Methods and the Grid-Forming Control

## 2.1 Overview of passive island detection methods

There are four main types of passive IDMs: voltage magnitude-based, frequency-based, voltage vector shift (VVS)-based, and composite method [23]–[29]. The voltage magnitude-based IDM measures the voltage at the IBR connection point and compares the measured voltage with a pre-defined threshold for identifying an islanding event. Thus, the voltage magnitude-based method is very sensitive to grid voltage dip and cannot be used on its own.[41] The frequency-based method uses the rate of change of frequency (RoCoF), frequency deviation ($\Delta f$), or accumulated rotor angle change due to frequency as a measure for island detection. The RoCoF-based method is sensitive to measurement noise [42] and is not favored in practice, whereas $\Delta f$-based method is one of the most typical IDMs used in practice as it is free from the derivative problem observed in the RoCoF-based method. The rotor-angle-deviation ($\Delta\theta_{\mathrm{r}}$) based method utilizes the integration of the frequency deviation $\Delta f$. [24], and is less sensitive to measurement noise than the $\Delta f$-based method.

The composite islanding detection method combines the classical VVS-based and $\Delta\theta_{\mathrm{r}}$-based IDM [25]. The VVS-based method is first used to detect an initial change in the angle of the voltage vector that may be caused by an islanding event whereas the $\Delta\theta_{\mathrm{r}}$ is then used to confirm an actual islanding event if it exceeds its threshold. As compared to the VVS-based IDM, the composite one has a smaller NDZ and is less prone to misdetection of grid phase angle jump and load switching as an island [25]. Table 2.1 summarizes the performance of five common passive IDMs in terms of sensitivity to noise, grid frequency variation, grid phase angle jump, island detection time, and NDZ. It is observed from Table 2.1 that the use of classical VVS- and $\Delta\theta_{\mathrm{r}}$- based IDM together provides more reliable island detection with smaller NDZ than the other passive IDMs. In this work, the composite method is the default passive IDM evaluated unless otherwise stated.

**Table 2.1:** Performance comparison of RoCoF-, f-, and VVS- based island detection

| **Island detection based on** | **Sensitivity to noise** | **Sensitivity to grid frequency variation** | **Sensitivity to grid phase angle jump** | **Island detection time for large exchange power** | **NDZ** |
|---|---|---|---|---|---|
| **RoCoF (Averaged over 500/100 ms)** | High | High | Low | High | Medium |
| **f (Averaged over 500/100 ms)** | Medium | High | Low | High | Medium |
| **Classical VVS** | Low | Medium | High | Low | Medium |
| **Rotor angle deviation** | Low | High | Low | Medium | Medium |
| **Composite (VVS + rotor angle deviation)** | Low | Low | Low | Medium | Low |

## 2.2 Grid-forming control for inverter-based resources

### 2.2.1 Overview of active-power based synchronization strategies

One of the methods to implement the GFM control is to calculate the synchronizing angle of a GFM controller through an active power control loop. In the literature, there are different active power controller structures for the GFM control. Fig. 2.1 lists five available active power controller structures for obtaining the synchronization angle in the literature: droop control [34], [36], proportional droop controller with a low-pass filter (LPF) [37], power synchronization control (PSC) [43], PI-based controller [44], and virtual synchronous machine (VSM) control [34], [43], [44]. The droop control in Fig. 2.1(a) and the power synchronization control in Fig. 2.1(c) implement a single integrator to acquire the synchronization angle from the active power mismatch. The grid base rotating frequency is expressed as $\omega_0$ in p.u. and $\omega_\mathrm{b}$ in rad/s. The two GFM control structures are simple to implement but do not provide inertial responses on their own. To provide virtual inertia, the droop control in Fig. 2.1(a) is modified to include a low pass filter as in Fig. 2.1(b), which represents a second-order transfer function and uses two integrals to obtain the synchronization angle from the power mismatch. Fig. 2.1(d) uses a PI-based GFM control together with a low pass filter to obtain the synchronization angle from the active power mismatch. Fig. 2.1(e) represents the VSM control which obtains the synchronization angle by emulating the swing equation of a synchronous generator with added speed damping.

The droop control with a low pass filter in (b) is mathematically equivalent to the VSM control in the absence of the high pass filter in the damping. Furthermore, the PI-based GFM control is equivalent to the VSM controller if the closed-loop transfer function of the active power controller is loop-shaped to a $3^{\mathrm{rd}}$ order system with identical poles [44]. Moreover, the droop controller in (a) and power synchronization control in (c) are also special cases of VSM control providing no virtual inertia. The VSM control is implemented according to the structure of a swing equation using inertia constant and damping constant and does not require grid angle estimation, e.g. through a PLL, for the synchronization purpose. As described above, the VSM controller struc-

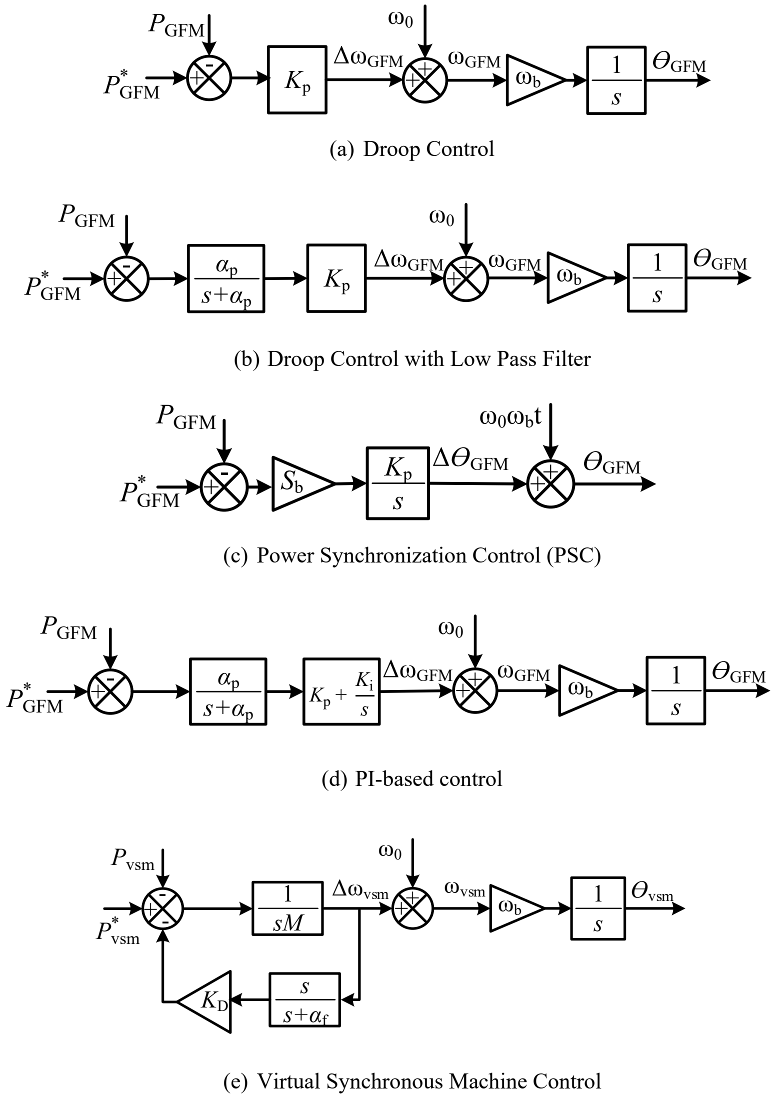


(a) Droop Control

(b) Droop Control with Low Pass Filter

(c) Power Synchronization Control (PSC)

(d) PI-based control

(e) Virtual Synchronous Machine Control

**Figure 2.1:** GFM control structures using active power based synchronization strategy

ture is more general or equivalent to the other controller structures [35], hence the VSM control structure described in [45] is selected for implementing the GFM control in this thesis.

### 2.2.2 Virtual synchronous machine-based grid-forming control of battery energy storage system

In an MG powered by renewables, a battery energy storage system (BESS) may be used to control the voltage and frequency of the microgrid during island operation. Fig. 2.2 shows the complete controller for the BESS implemented, including the frequency controller, the VSM-based active power controller, the voltage controller, and the inner current controller.

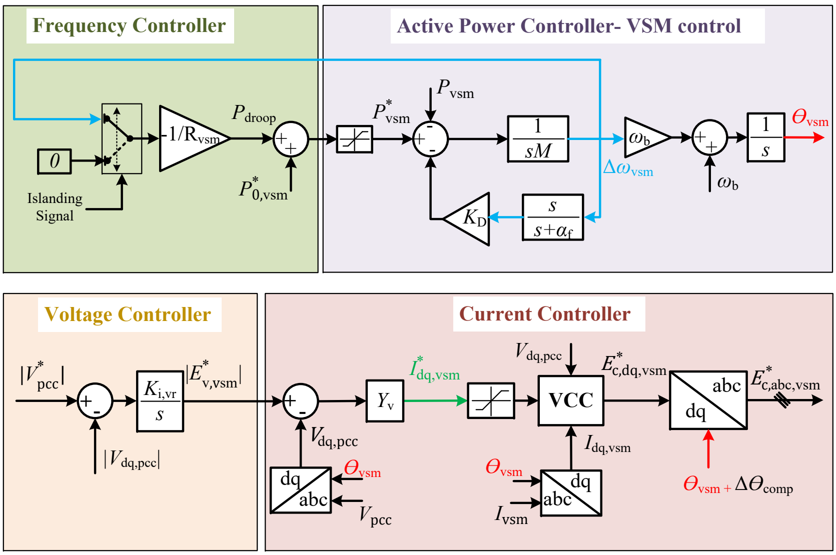


**Figure 2.2:** Block diagram of controllers for VSM

The frequency controller uses a proportional droop of $1/R_{\text{vsm}}$. The VSM calculates the rotational frequency $\omega_{\text{vsm}}$ and the synchronization angle $\theta_{\text{vsm}}$ based on the power balance between the reference power $P^*_{\text{vsm}}$ and the actual

electrical power $P_{\mathrm{vsm}}$ output from the BESS, where M is twice the virtual inertia constant, and the virtual damping is implemented by a damping constant $K_{\mathrm{D}}$ and the high-pass filter with the cut-off frequency of $\alpha_{\mathrm{f}}$ [45]. The voltage controller is implemented as an integrator with the gain of $K_{\mathrm{i,vr}}$, and controls the voltage $V_{\mathrm{pcc}}$ at the point of common coupling (PCC) between the BESS and the local grid. $E_{\mathrm{v,vsm}}$ is the virtual back EMF of the VSM and $Y_{\mathrm{v}}$ is the virtual admittance.
In steady state,

$$\bar{E}_{\mathrm{vsm}} = \frac{\bar{I}_{\mathrm{vsm}}}{Y_{\mathrm{v}}} + \bar{V}_{\mathrm{pcc}}, \tag{2.1}$$

where

$$Y_{\mathrm{v}} = \frac{1}{R_{\mathrm{v}} + sL_{\mathrm{v}} + j\omega_{\mathrm{b}} L_{\mathrm{v}}}, \tag{2.2}$$

$R_{\mathrm{v}}$ and $L_{\mathrm{v}}$ are the virtual resistance and inductance of the VSM, respectively. $I_{\mathrm{vsm}}$ is the measured current injected to the grid from the BESS and $I^*_{\mathrm{vsm}}$ is the corresponding reference current, whose magnitude is limited to the inverter current rating. The current controller calculates the resulting reference dq voltage of the inverter $E^*_{\mathrm{c,vsm}}$. The virtual impedance is the equivalent impedance seen by the virtual back EMF before the PCC voltage. The purpose of the virtual resistance is to improve the damping of the dc component of the output current; whereas the use of virtual reactance makes the voltage controller parameter tuning less sensitive to grid impedance [44]. It is worth mentioning that the use of virtual impedance does not introduce additional losses in the physical system.

## 2.3 Summary

Passive island detection methods (IDMs) i.e. frequency-based, voltage vector shift (VVS)-based, and composite method are reviewed and compared based on the different performance parameters for secure grid connected operation and fast and accurate island detection. The composite IDM that combines the VVS-based and rotor-angle-deviation based IDM is more advantageous than the other passive methods. Furthermore, for implementing GFM control for an IBR in the thesis the VSM-based GFM control structure design is selected for implementation in this thesis as other active power based synchronization strategies are either special cases or have equivalence to the VSM-based GFM control structure.

# CHAPTER 3

## Passive Island Detection for Grid-Forming Inverter

### 3.1 Proposed PQ-based load angle estimation

The classical VVS-based IDM estimates the voltage angle jump typically by using dq transformation or discrete fourier transform of the terminal voltage of the IBR. For the VSM-based GFM control, the voltage angle jump at the terminal of the inverter is equivalent to the load angle jump of the inverter as the rotor angle of the virtual back EMF of the inverter does not change immediately. Hereafter, the IBR with a VSM-based GFM controller will be referred to as VSM for simplicity. In this work, the load angle ($\delta$) between the virtual back EMF of VSM and the PCC voltage will be used instead of the terminal voltage angle for analyzing VVS-based IDM. Furthermore, in case the virtual impedance is not used, the actual RL filter impedance is highly inductive. This implies that the reactive power imbalance in the MG during an islanding event will not have a significant impact on the phase angle jump of the PCC voltage. However, the analysis below is valid for cases with and without virtual impedance.

From 2.1,

$$\bar{E}_{\mathrm{vsm}} = R_{\mathrm{v}} \bar{I}_{\mathrm{vsm}} + jX_{\mathrm{v}} \bar{I}_{\mathrm{vsm}} + \bar{V}_{\mathrm{pcc}}. \tag{3.1}$$

Fig. 3.1 illustrates the corresponding phasor diagram according to (3.1). In case of an islanding event, for a slow varying virtual back emf, the sudden change in the current phasor $\bar{I}_{\mathrm{vsm}}$ through the BESS results in a PCC voltage phasor $\bar{V}_{\mathrm{pcc}}$ shift. With the selected control, the virtual back EMF, both right before ($E_{\mathrm{vsm}}$) and right after ($E'_{\mathrm{vsm}}$) the islanding event, is aligned on the d-axis of the dq-coordinate as $E_{\mathrm{vsm,q}}$ =0. The current phasor shifts from $I_{\mathrm{vsm}}$ to $I'_{\mathrm{vsm}}$, which leads to the angle shift of $\Delta\theta_{\mathrm{init}}$ at the PCC voltage from $V_{\mathrm{pcc}}$ to $V'_{\mathrm{pcc}}$. Accordingly, the load angle of the VSM shifts from $\delta$ to $\delta'$.

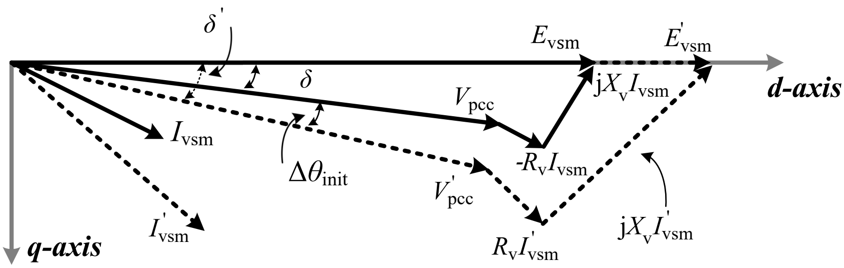


**Figure 3.1:** Initial angle jump of PCC voltage right after the islanding event

According to the phasor diagram method, given the measured active ($P_{\mathrm{vsm}}$) and reactive power ($Q_{\mathrm{vsm}}$) output of the VSM, the load angle $\delta$ can be estimated as,

$$\delta = \tan^{-1}\left(\frac{b}{1+a}\right), \tag{3.2}$$

where,

$$a = \frac{R_{\mathrm{v}} P_{\mathrm{vsm}} + X_{\mathrm{v}} Q_{\mathrm{vsm}}}{|V_{\mathrm{pcc}}|^2} \tag{3.3a}$$

$$b = \frac{X_{\mathrm{v}} P_{\mathrm{vsm}} - R_{\mathrm{v}} Q_{\mathrm{vsm}}}{|V_{\mathrm{pcc}}|^2}. \tag{3.3b}$$

For real-time implementation, we propose to use (3.2) and (3.3) to estimate the load angle $\delta$ , and thus the corresponding cycle-to-cycle load angle jump ($\Delta\delta_{\mathrm{init}}(t)$) for VVS-based IDM. Hence in continuous time,

$$\Delta\delta_{\mathrm{init}}(t) = \delta^{'} - \delta(t - T_{\mathrm{n}}), \tag{3.4}$$

where $T_{\mathrm{n}}$ is the rated electrical period, i.e. 20 ms in a 50 Hz grid. If the obtained value of the $\Delta\delta_{\mathrm{init}}$ is greater than the threshold, the estimation of the rotor angle deviation ($\Delta\theta_{\mathrm{r}}$) is triggered. The $\Delta\theta_{\mathrm{r}}$ is a result of frequency deviation due to the mismatch between the measured and reference active power. Since the $\Delta\delta_{\mathrm{init}}$ is used only for triggering the $\Delta\theta_{\mathrm{r}}$ estimation, the threshold can be selected to a very low value of 1° [25].

For a given threshold of $\Delta\delta_{\mathrm{init}}$, the NDZ for active and reactive power change by using VVS-based IDM can be estimated. Rearranging (3.2) and (3.3) and solving for active and reactive power give

$$P_{\mathrm{vsm}} = \frac{V_{\mathrm{pcc}}^2 \tan(\delta) + Q_{\mathrm{vsm}}[X_{\mathrm{v}} \tan(\delta) + R_{\mathrm{v}}]}{X_{\mathrm{v}} - R_{\mathrm{v}} \tan(\delta)} \tag{3.5}$$

Assume a relatively small load angle change such that $\tan(\delta) \approx \delta$. For a first-order linearization around the initial operating point,$P_{0,\mathrm{vsm}}$, $Q_{0,\mathrm{vsm}}$, $|V_{0,\mathrm{pcc}}|$ and $\delta_0$, the NDZ when subject to a change in the active power $\Delta P_{\mathrm{vsm}}$ and reactive power $\Delta Q_{\mathrm{vsm}}$ at the VSM terminal can be approximated by

$$\Delta P_{\mathrm{vsm}} = K_1 \Delta Q_{\mathrm{vsm}} + K_2 \Delta V_{\mathrm{pcc}} + K_3 \Delta\delta_{\mathrm{init}}^{\mathrm{th}}, \tag{3.6}$$

where

$$K_1 = \frac{\frac{R_{\mathrm{v}}}{X_{\mathrm{v}}} + \delta_0}{1 - \frac{R_{\mathrm{v}}}{X_{\mathrm{v}}}\delta_0}, \tag{3.7a}$$

$$K_2 = \frac{2\,|V_{0,\mathrm{pcc}}|\,\delta_0}{X_{\mathrm{v}} - R_{\mathrm{v}}\delta_0}, \tag{3.7b}$$

$$K_3 = \frac{\frac{|V_{0,\mathrm{pcc}}|^2}{X_{\mathrm{v}}} + \frac{R_{\mathrm{v}}}{X_{\mathrm{v}}} P_{0,\mathrm{vsm}} + Q_{0,\mathrm{vsm}}}{1 - \frac{R_{\mathrm{v}}}{X_{\mathrm{v}}}\delta_0}, \tag{3.7c}$$

and $\Delta\delta_{\mathrm{init}}^{\mathrm{th}}$ is the threshold of the cycle-to-cycle load angle jump. The relation shows that the slope of the $\Delta P_{\mathrm{vsm}}$ vs $\Delta Q_{\mathrm{vsm}}$ NDZ plot is primarily determined by the R/X ratio of the virtual impedance in $K_1$ at a given operating point. Whereas $K_3$ defines the y-intercept value and hence the area of the NDZ for a

$\pm\Delta\delta_{\text{init}}^{\text{th}}$ when $\Delta V_{\text{pcc}}$ =0. For a small initial operating point of $P_{0,\text{vsm}}$, $Q_{0,\text{vsm}}$, and $\delta_0$ the area of the NDZ depends inversely on the virtual reactance in $K_3$. To further analyze and illustrate the NDZ in the active and reactive power mismatch space for $\Delta P_{\text{vsm}}$ and $\Delta Q_{\text{vsm}}$ at the VSM terminal, three cases are selected and the NDZ is calculated using (3.6):

1. Low $R_{\text{v}}$-low $X_{\text{v}}$: $Z_{\text{v}} = 0.015 + j0.15$ p.u.,
2. Low $R_{\text{v}}$-high $X_{\text{v}}$: $Z_{\text{v}} = 0.015 + j0.5$ p.u.,
3. High $R_{\text{v}}$-high $X_{\text{v}}$: $Z_{\text{v}} = 0.25 + j0.5$ p.u..

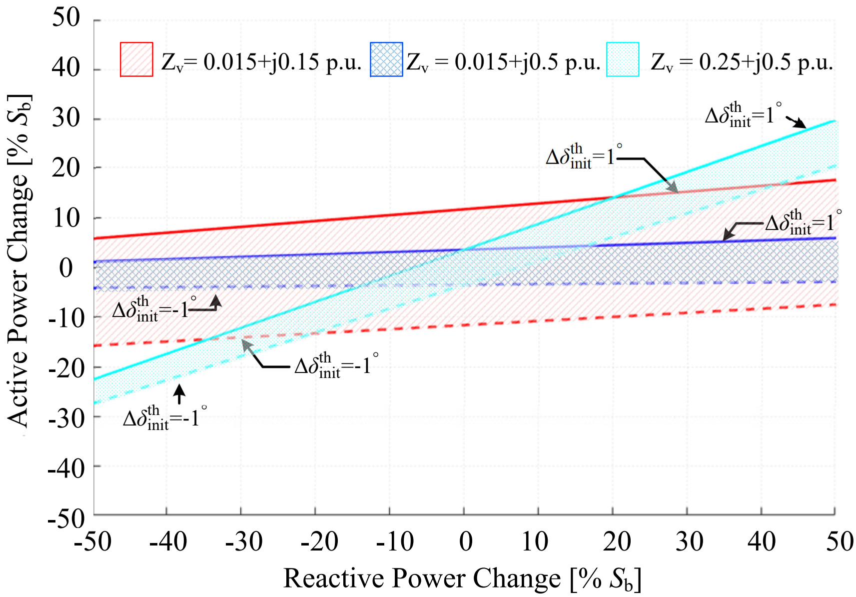


**Figure 3.2:** Non-detection zone of VVS-based island detection method at different virtual impedance.

Fig. 3.2 shows the resulting NDZ of the selected three virtual impedances. As the virtual reactance is increased from 0.15 p.u. (in red and slanted pattern fill) to 0.5 p.u. (in blue with a square pattern fill) , $K_1$ and $K_3$ are reduced, decreasing the slope and the area of the NDZ. This is in accordance with the linearized formula derived in (3.6). On the other hand, when the virtual resistance is increased from 0.015 p.u. (in blue with a square pattern fill) to 0.25 p.u. (in cyan and dotted pattern fill), the R/X ratio increases, and thus the slope of the NDZ, $K_1$ also increases. However, the area of the NDZ remains more or less unchanged as it depends largely on the virtual reactance, which remains unchanged. This implies that a higher virtual reactance tends to reduce the NDZ of the VVS-based IDM and a high R/X ratio of the virtual impedance tends to shift the NDZ of $\Delta P$ upwards as $\Delta Q$ increases.

## 3.2 On relation between island detection time and controller parameters of the VSM

Frequency-based IDM is another typical method for detecting an islanding event based on the swing equation of a synchronous generator. Once the VVS detects a sufficiently large load angle jump, the rotor angle deviation $\Delta\theta_{\mathrm{r}}$, which is the accumulation of the frequency deviation $\Delta f$ is used for confirming an islanding event. This subsection derives analytical expressions of $\Delta f$ and $\Delta\theta_{\mathrm{r}}$ as a function of the controller parameters of VSM. This is particularly useful when determining the selection of the threshold of $\Delta f$ or $\Delta\theta_{\mathrm{r}}$ for island detection to meet the required island detection time at a given power disturbance.

The VSM controller emulates the swing equation of a synchronous machine to determine the synchronizing angle according to [45] as:

$$2H_{\mathrm{vsm}}\frac{d\Delta\omega_{\mathrm{vsm}}}{dt} = P^{*}_{\mathrm{vsm}} - P_{\mathrm{vsm}} - D_{\mathrm{vsm}}(t)\Delta\omega_{\mathrm{vsm}} \tag{3.8}$$

where

$$D_{\mathrm{vsm}}(s) = \mathcal{L}\{D_{\mathrm{vsm}}(t)\} = K_{\mathrm{D}}\frac{s}{s+\alpha_{\mathrm{f}}}. \tag{3.9}$$

Before the islanding event, the electrical power output from the BESS $P_{0,\mathrm{vsm}} = P^{*}_{0,\mathrm{vsm}}$. At the instant of an islanding event, the active power output from the BESS is increased by $\Delta P_{\mathrm{vsm}}$ from $P^{*}_{0,\mathrm{vsm}}$ to $P_{\mathrm{vsm}}$ for keeping the local power balance, i.e.

$$P_{\mathrm{vsm}} = P^{*}_{0,\mathrm{vsm}} + \Delta P_{\mathrm{vsm}}. \tag{3.10}$$

Substituting (3.10) into (3.8) gives,

$$2H_{\mathrm{vsm}}\frac{d\Delta\omega_{\mathrm{vsm}}}{dt} = -\Delta P_{\mathrm{vsm}} - D_{\mathrm{vsm}}(t)\Delta\omega_{\mathrm{vsm}}. \tag{3.11}$$

In the s-domain, (3.11) becomes,

$$2H_{\mathrm{vsm}}s\Delta\omega_{\mathrm{vsm}}(s) = -\Delta P_{\mathrm{vsm}}(s) - D_{\mathrm{vsm}}(s)\Delta\omega_{\mathrm{vsm}}(s). \tag{3.12}$$

The transfer function of the VSM frequency with respect to the electrical power output becomes,

$$\frac{\Delta\omega_{\mathrm{vsm}}(s)}{\Delta P_{\mathrm{vsm}}(s)} = \frac{-1}{2H_{\mathrm{vsm}}s + D_{\mathrm{vsm}}(s)}. \tag{3.13}$$

Substituting value for $D_{\mathrm{vsm}}(s)$ from equation (3.9) in (3.13)

$$\frac{\Delta\omega_{\mathrm{vsm}}(s)}{\Delta P_{\mathrm{vsm}}(s)} = \frac{-1}{2H_{\mathrm{vsm}}s + K_{\mathrm{D}}\frac{s}{s+\alpha_{\mathrm{f}}}}. \tag{3.14}$$

For a step change in $\Delta P_{\mathrm{vsm}}$, i.e. $\Delta P_{\mathrm{vsm}}(s) = \Delta P_{\mathrm{vsm}}/s$ the time domain response of the VSM frequency becomes,

$$\Delta\omega_{\mathrm{vsm}}(t) = \frac{-\Delta P_{\mathrm{vsm}}T_{\mathrm{D}}}{2H_{\mathrm{vsm}}}\left[\alpha_{\mathrm{f}}t + (1-\alpha_{\mathrm{f}}T_{\mathrm{D}})(1-e^{-\frac{t}{T_{\mathrm{D}}}})\right], \tag{3.15}$$

where

$$T_{\mathrm{D}} = \frac{1}{\alpha_{\mathrm{f}} + \frac{K_{\mathrm{D}}}{2H_{\mathrm{vsm}}}} \tag{3.16}$$

Accordingly, the rotor angle of the VSM will deviate from its initial value by,

$$\Delta\theta_{\mathrm{r}}(t) = \int_0^t \omega_{\mathrm{b}}\Delta\omega_{\mathrm{vsm}}(t)\,dt.$$

Therefore,

$$\Delta\theta_{\mathrm{r}}(t) = \frac{-\Delta P_{\mathrm{vsm}}T_{\mathrm{D}}\omega_{\mathrm{b}}}{2H_{\mathrm{vsm}}}\left[\frac{\alpha_{\mathrm{f}}}{2}t^2 + (1-\alpha_{\mathrm{f}}T_{\mathrm{D}})(t + T_{\mathrm{D}}e^{-\frac{t}{T_{\mathrm{D}}}} - T_{\mathrm{D}})\right]. \tag{3.17}$$

Equations (3.15) and (3.17) calculate the frequency and rotor angle deviation of the VSM over time when subject to an active power imbalance. Both deviations depend on not only the active power imbalance but also the virtual inertia and damping of the VSM. The relation in (3.15) or (3.17) can be used to calculate the island detection time given an active power imbalance and a threshold value of $\Delta\omega_{\mathrm{vsm}}$ or $\Delta\theta_{\mathrm{r}}$. On the other hand, the relation can also be used to set the threshold value of $\Delta\omega_{\mathrm{vsm}}$ (for $\Delta f$-based IDM) or $\Delta\theta_{\mathrm{r}}$ (for $\Delta\theta_{\mathrm{r}}$-based IDM) given the controller parameters of VSM and active power imbalance at a desired island detection time.

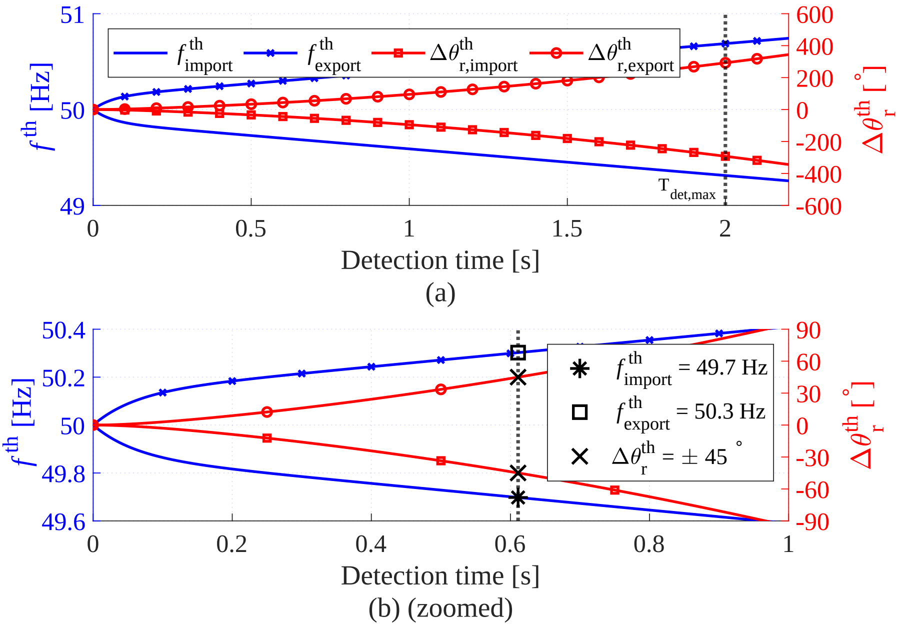


**Figure 3.3:** Equivalent threshold settings for $\Delta f$-based and $\Delta\theta_{\mathrm{r}}$- based island detection for $\Delta P_{\mathrm{vsm}} = \pm$ 30% $S_{\mathrm{b}}$, $H_{\mathrm{vsm}} = 3$ s, $K_{\mathrm{D}} = 89.40$ p.u., $\alpha_{\mathrm{f}} =$ 1.86 rad/s.

Fig. 3.3 shows the threshold settings for $\Delta f$-based (left-hand side y-axis) and $\Delta\theta_{\mathrm{r}}$-based IDM (right-hand side y-axis) for a required island detection time at a power mismatch of 0.3 p.u., based on the BESS rating in both the active power import and export case. $T_{\mathrm{det,max}}$ represents the maximum island detection time limit of 2 s recommended in [40]. The $H_{\text{vsm}}$ is selected as 3 s and values of $K_{\text{D}}$ and $\alpha_{\text{f}}$ are designed based on the tuning presented in [44]. Fig. 3.3 shows that the two methods are theoretically equivalent to each other if their threshold values are set accordingly. Fig 3.3 (b) shows an example where the threshold setting of $|\Delta\theta_{\text{r}}^{\text{th}}| = 45°$ is used for $\Delta\theta_{\text{r}}$-based IDM. For a 0.3 p.u. active power imbalance, the resulting island detection time is $T_{\text{det}} = 0.611$ s. The same island detection time can also be achieved for a $\Delta f$-based IDM with a frequency threshold setting of $|\Delta f^{\text{th}}| = 0.3$ Hz.

## 3.3 Implementation of the composite island detection method

To be able to implement the controllers in dSPACE later for lab experiments, the controller and the selected composite IDM is implemented in a discrete-time domain. The following section describes the implementation of the VVS-based and $\Delta\theta_{\text{r}}$-based composite IDM in MATLAB/Simulink.

### 3.3.1 Estimation of cycle-to-cycle load angle jump

Fig. 3.4 (a) shows the estimation of the initial load angle jump $\Delta\delta_{\text{init}}$ in discrete simulation. The load angle here refers to the angle between the virtual back EMF and the PCC voltage of the BESS converter. The $\Delta\delta_{\text{init}}$ is estimated as the change of this load angle at the current electrical cycle with respect to the previous one, i.e.

$$\Delta\delta_{\text{init}}(i) = \delta(i) - \delta(i-1) \tag{3.18}$$

where $i = \text{floor}[((k-1)T_{\text{s}}/T_{\text{n}}) + 1]$. Once K = 1, the estimation of the rotor angle deviation $\Delta\theta_{\text{r}}$ will be initiated according to Fig. 3.4 (b).

### 3.3.2 Estimation of rotor angle deviation

Once the initial load angle jump $\Delta\delta_{\text{init}}$ exceeds its threshold $\Delta\delta_{\text{init}}^{th}$, a trigger signal 'K' is sent to start the calculation of the rotor angle deviation $\Delta\theta_{\text{r}}$, due to the change of the VSM frequency $\omega_{\text{vsm}}$ from its pre-disturbance value $\omega_{0,\text{vsm}}$. The $\omega_{0,\text{vsm}}(k)$ is the five-cycle average value of the frequency before receiving the trigger signal, and is calculated according to,

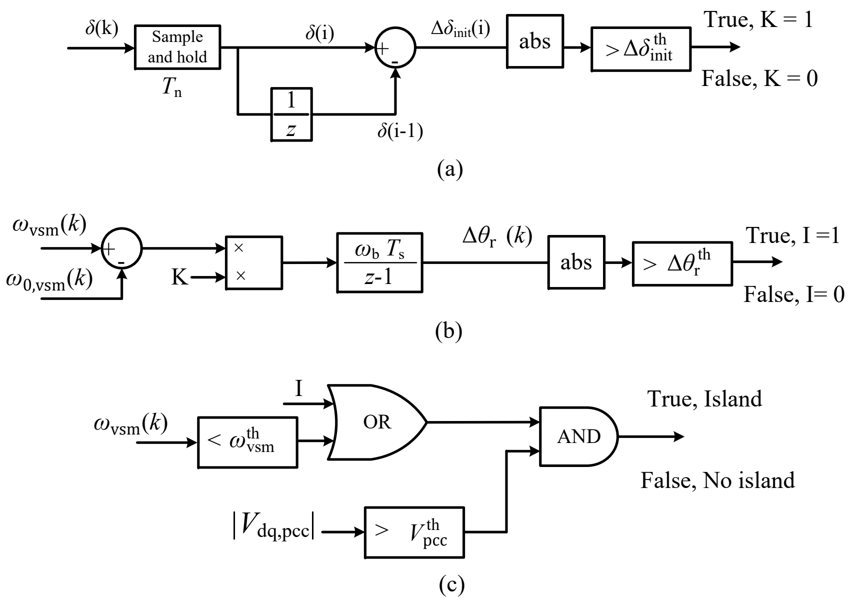


**Figure 3.4:** Implementation of composite passive island detection method

$$\omega_{0,\mathrm{vsm}}(k) = \frac{T_\mathrm{s}}{5T_\mathrm{n}} \sum_{i=k-\frac{5T_\mathrm{n}}{T_\mathrm{s}}}^{k-1} \omega_\mathrm{vsm}(i) \tag{3.19}$$

When the rotor angle deviation $\Delta\theta_\mathrm{r}$ accumulated reaches the selected threshold $\Delta\theta_\mathrm{r}^\mathrm{th}$, the true 'I' signal is used as an island signal when the PCC voltage is above the selected threshold which is achieved using the AND logic as shown in Fig. 3.4 (c). The island signal obtained is then used to activate the frequency controller of the BESS to regulate the frequency of the islanded MG. In practice, other actions such as shedding of non-critical loads and/or change of protection setting may also need to be carried out once an island is detected.

### 3.3.3 Frequency signal as a backup and voltage based blocking

Fig. 3.4 (c) shows the final composite passive island detection method deployed in this paper. In case of a very small active power mismatch during the island transition, $\Delta\delta_\mathrm{init}$ will be lower than the selected threshold of 1° and $\Delta\theta_\mathrm{r}$ will not be activated. This corresponds to the NDZ of the VVS-based IDM. However, MG frequency may start to drift away due to a small power imbalance in the islanded MG. Thus it is important to use the $\Delta f$-based IDM as a backup signal for island detection. This will reduce the NDZ of the composite VVS-based method caused by the $\Delta\delta_\mathrm{init}$. Furthermore, a simple voltage magnitude-based blocking of the islanding signal is implemented to avoid misdetection of grid faults as islanding events. On the other hand, the MG is expected to isolate itself (island) for an occurrence of a fault on the grid side. This can be achieved by bi-directional overcurrent relays or by sending a breaker disconnection signal obtained from a fault detection algorithm. However, this is not the focus of the thesis, and will not be further discussed.

## 3.4 Summary

This chapter has summarized the theories for analyzing the performance of passive IDMs for a microgrid powered by IBRs with VSM-based GFM control. The main takeaways include:

- The proposed PQ-based load angle estimation method is discussed in detail for estimating the load angle jump when subject to a power mismatch at the terminal of the inverter. The non-detection zone (NDZ) of the VVS-based IDM is also expressed analytically.
- It is observed that the area of NDZ primarily depends on the virtual reactance for a selected threshold of cycle-to-cycle load angle jump if the initial active and reactive power operating points of the VSM are zero.
- The slope of NDZ is defined mainly by the R/X ratio of the virtual impedance.
- An analytical expression defining the relation between island detection time and VSM controller parameters for both the $\Delta f$-based and $\Delta\theta_{\mathrm{r}}$-based IDM is derived and compared. The two methods can be equivalent to each other if their corresponding threshold settings are selected accordingly.

CHAPTER 4

# Case Study and Simulation Results

## 4.1 Description of case study

Fig. 4.1 shows the electrical diagram of a medium-voltage distribution grid connected to the main grid.

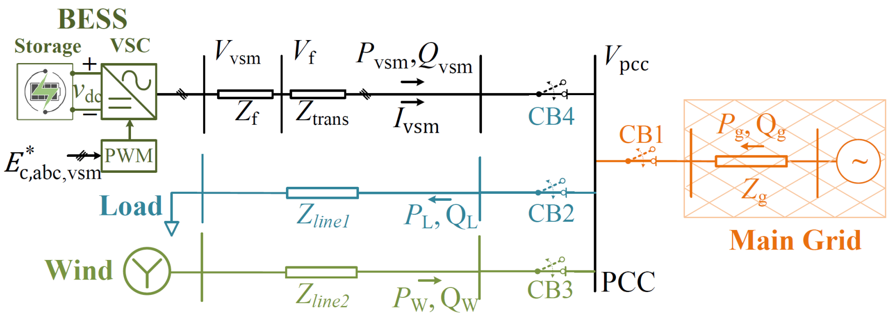


**Figure 4.1:** Single Line Diagram- Case Study System

The distribution grid supplies the local community load together with the local wind power generation. A BESS is installed to mitigate the increased peak load and to improve the supply reliability of the local community. Table 4.1 summarizes the parameters of the grid, a BESS, wind turbines, and load. The constant power load is implemented in the simulation using the 'Three-Phase Dynamic Load' block from Simulink [46]. There are 5 variable speed wind turbines each rated 2 MW. and are modelled as an aggregated negative load in the simulation. The settings of the VVS-based and the accumulated rotor angle change-based IDM is also included in the table.

**Table 4.1:** Case study system parameters

| **Grid Parameters** | **Values** |
|---|---|
| Short circuit ratio, SCR | 3 |
| X/R ratio | 10 |
| Base grid rotational frequency, $\omega_\mathrm{b}$ | $2\pi \times 50$ rad/s |
| **BESS Parameters** | |
| Rated BESS Power, $S_\mathrm{b}$ | 10 MVA |
| Rated BESS grid voltage (L-L,RMS), $V_\mathrm{LL}$ | 11 kV |
| Filter impedance, $Z_\mathrm{f}$ | $0.009 + j0.09$ p.u. |
| Transformer impedance, $Z_\mathrm{trans}$ | $0.006 + j0.06$ p.u. |
| Virtual resistance, $R_\mathrm{v}$ | 0.25 p.u. |
| Virtual inductance, $L_\mathrm{v}$ | 0.5 p.u. |
| Frequency droop, $R_\mathrm{vsm}$ | 0.04 p.u. |
| Virtual inertia constant , $H_\mathrm{vsm}$ | 3 s |
| Virtual damping constant , $K_\mathrm{D}$ | 89.4 p.u. |
| High pass filter bandwidth , $\alpha_\mathrm{f}$ | 1.8625 rad/s |
| Voltage controller bandwidth , $\alpha_\mathrm{vc}$ | $2\pi \times 12.732$ rad/s |
| Voltage controller integral gain , $K_\mathrm{i,vc}$ | 200 rad/s |
| Current controller bandwidth , $\alpha_\mathrm{cc}$ | $2\pi \times 500$ rad/s |
| Current controller proportional gain , $K_\mathrm{p,cc}$ | 1.5 p.u. |
| Current controller integral gain , $K_\mathrm{i,cc}$ | 47.124 rad/s |
| **Wind generators rating** | |
| Installed capacity, $S_\mathrm{w}$ | 5×2.13 MVA, $\cos\phi = 0.94$ |
| Maximum active power, $P_\mathrm{w,max}$ | 5×2 MW |
| **Island detection settings** | |
| Initial voltage angle jump threshold , $\lvert\Delta\theta_\mathrm{init}\rvert$ | 1° |
| Accumulated rotor angle change threshold , $\lvert\Delta\theta_\mathrm{r}\rvert$ | 45° |
| **Load Parameters** | |
| Rated load power (10% Constant impedance + 90% Constant power load) | 10 MVA $\cos\phi = 1$ |

## 4.2 Base case scenario

For the base case in the simulation studies, the values of controller parameters for VSM follow Table 4.1. Fig. 4.2 shows the steady state power flow before and after the islanding event for the base case scenario.

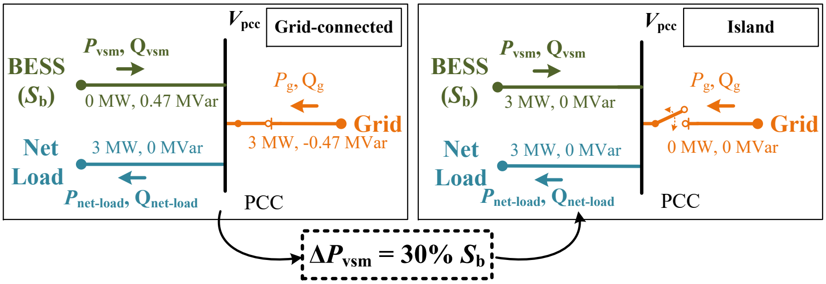


**Figure 4.2:** Power flow before and after island for the base case scenario. $P_{net-load} = P_{load} - P_w$ = 10 MW - 7 MW = 3 MW.

Fig.4.3 (a) and (b) show the dynamic response of the electrical power output from the BESS and the microgrid frequency when the microgrid is disconnected from the main grid at t= 1 s. Prior to the islanding event, wind turbines were generating 7 MW (0.7 p.u.) of power and the remaining 3 MW (0.3 p.u.) was imported from the grid. When the microgrid is disconnected from the grid, this net load power of 3 MW (0.3 p.u.) is drawn from the BESS to handle the power imbalance in the microgrid. The frequency controller of the BESS is not enabled as the island transition is not yet detected. At the instant of the islanding event, as shown in Fig.4.3 (c), there is an initial load angle jump of $\Delta\delta_{\text{init}} = 7.5°$, which is larger than the threshold of $\pm 1°$. This triggers the calculation of the rotor angle deviation $\Delta\theta_r$, as shown in Fig.4.3 (d) which is caused by the declining frequency in the microgrid. The islanding event is eventually detected after about 0.7 s once the $\Delta\theta_r$ reaches the threshold of $\pm 45°$. Upon island detection, the frequency controller of the BESS is activated to stabilize the microgrid frequency. Prior to the activation, the frequency controller is frozen. This may not be the case if the BESS is expected to provide frequency reserve during the grid-connected case.

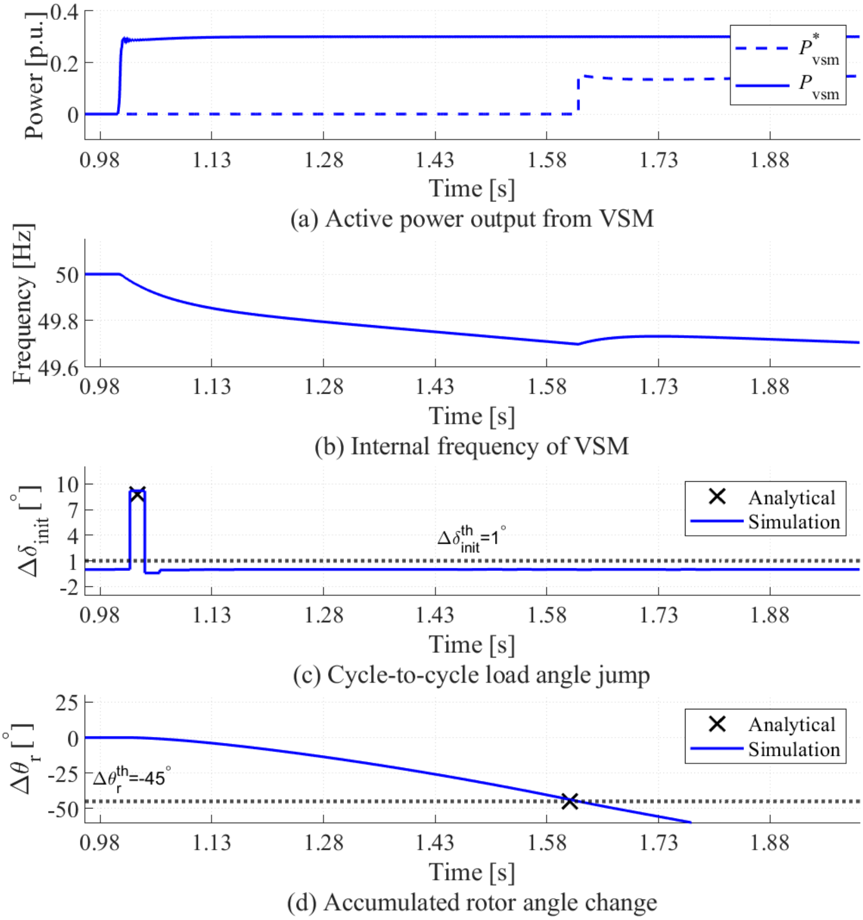


(a) Active power output from VSM

(b) Internal frequency of VSM

(c) Cycle-to-cycle load angle jump

(d) Accumulated rotor angle change

**Figure 4.3:** Unplanned island on the microgrid for $\Delta P_{\mathrm{vsm}} = 30\% S_{\mathrm{b}}$

## 4.3 PQ-based vs dq-based load angle estimation for voltage vector shift-based island detection method

Fig. 4.4 shows the PQ-based method for estimating the cycle-to-cycle load angle jump as compared to the dq-based estimation method. The grid import was 0.3 p.u prior to the islanding event at t = 1 s as shown in Fig. 4.2.

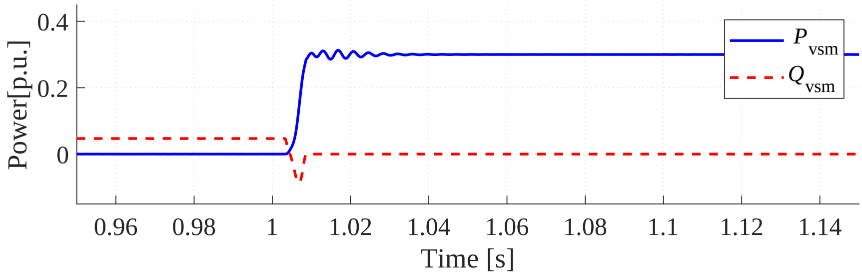

(a) Active and reactive power of the VSM

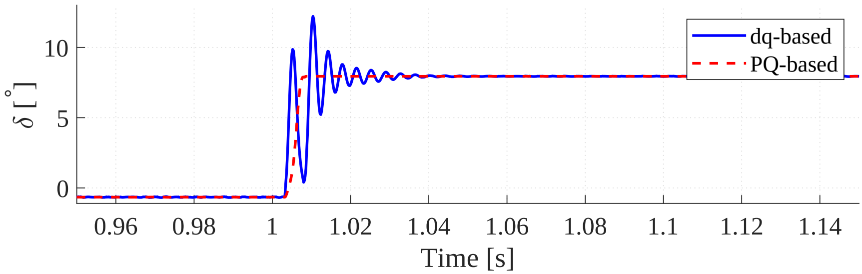

(b) dq-based vs PQ-based estimated load angle

**Figure 4.4:** Comparison of PQ-based and dq-based estimation of load angle for implementing VVS-based IDM for $\Delta P_{\text{vsm}} = 30\% S_{\text{b}}$

As shown in Fig. 4.4 (b), the dq-based estimation method captures the electrical transients of the voltage angle observed within an electrical cycle (blue curve). Hence the load angle estimated using the dq-based method is very sensitive to these electrical transients. On the other hand, the proposed method estimates the load angle according to (3.2), which is based on the phasor diagram, even though the active and reactive power measured are instantaneous quantities (dashed red curve). Therefore, the proposed method provides a more stable estimation of the load angle $\delta$ which will mitigate false triggering during the captured electrical transients.

## 4.4 Impact of control parameters of VSM on voltage vector shift-based island detection method

### 4.4.1 Impact of voltage controller gain

Fig. 4.5 shows the impact of the voltage controller integral gains and hence the bandwidth on the terminal voltage of the BESS, and the cycle-to-cycle load angle jump. The microgrid imports 0.3 p.u. of active power from the main grid as shown in Fig. 4.2 before the islanding event occurs at t = 1 s. The integral gain with a large value of 200 rad/s enables the voltage magnitude to recover back to 1 p.u. faster after the islanding event. The resulting cycle-to-cycle load angle jump $\Delta\delta_{\mathrm{init}}$ matches well with the analytical value indicated by '×' according to (3.2) - (3.4). In contrast, the estimated $\Delta\delta_{\mathrm{init}}$ becomes slightly larger in the case of a slower voltage regulator with an integral gain of 20 rad/s as the voltage magnitude $|V_{\mathrm{pcc}}|$ is now lower than 1 p.u. However, with the values selected for the case study, the difference is small and does not negatively affect the island detection.

### 4.4.2 Impact of filter parameter estimation error and its mitigation by virtual impedance

The physical implementation of a VSM may or may not involve a virtual impedance ($Z_{\mathrm{v}}$) [47]. However, if the virtual impedance is not used, the estimation of cycle-to-cycle load angle jump uses the impedance value of the physical RL filter, and the value may not be known perfectly. Such an error in the estimation of the filter impedance may affect the estimation accuracy of the cycle-to-cycle load angle jump. To evaluate this phenomenon, a small active power change of 0.12 p.u. is selected during the islanding event for the VSM with the power flow as shown in Fig. 4.6. Fig. 4.7 shows the resulting cycle-to-cycle load angle jump with/without virtual reactance. The estimated value of filter reactance is assumed to have a 10% error and is equal

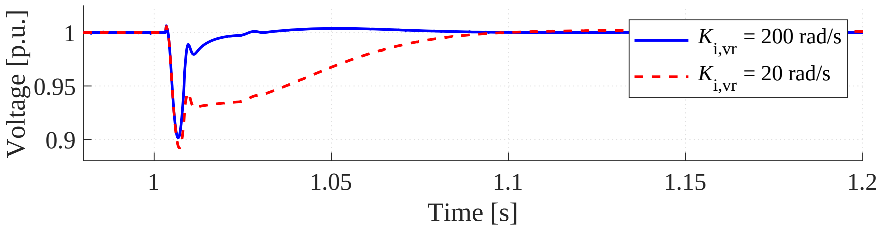


(a) PCC voltage magnitude

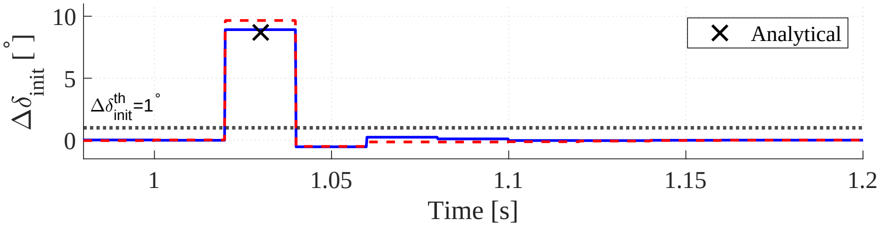


(b) Cycle-to-cycle load angle jump

**Figure 4.5:** Impact of two different voltage controller integral gains on the voltage magnitude and the cycle-to-cycle change in the load angle for $\Delta P_{\mathrm{vsm}} = 30\% S_{\mathrm{b}}$

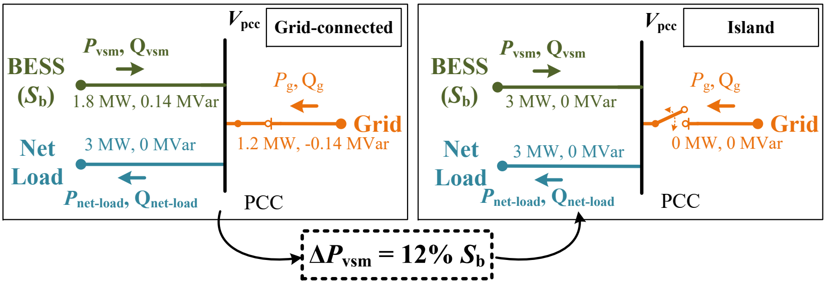


**Figure 4.6:** Power flows before and after the island to study the impact of parameter estimation error on $\Delta\delta_{\text{init}}$. $P_{\text{net-load}} = P_{\text{load}}$ - $P_{\text{w}}$ = 10 MW - 7 MW = 3 MW.

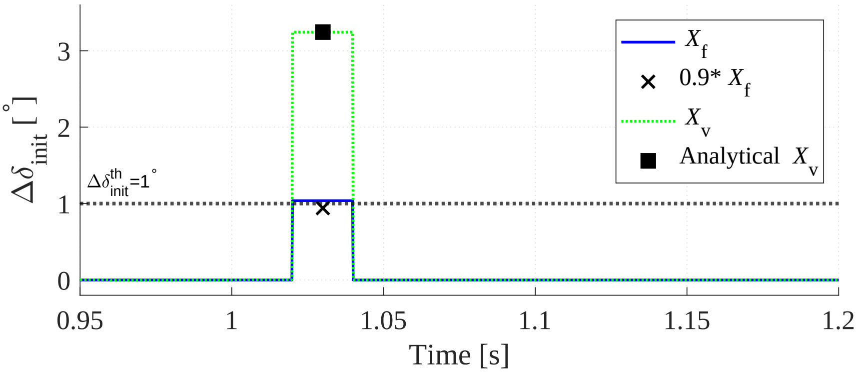


**Figure 4.7:** Cycle-to-cycle load angle jump for actual filter reactance ($X_{\text{f}}$), filter reactance with 10% error in parameter estimation, and virtual impedance for $\Delta P_{\text{vsm}} = 12\% S_{\text{b}}$

to 90% of the actual value $X_{\text{f}}$. When the virtual reactance is not used, the cycle-to-cycle load angle jump $\Delta\delta_{\text{init}}$ is 0.94° for an estimated value of $0.9X_{\text{f}}$. However, for the actual $X_{\text{f}}$, the $\Delta\delta_{\text{init}}$ is 1.04°, which is above the threshold of VVS-based IDM. This implies that the parameter estimation error affects the NDZ of the VVS-based IDM. On the other hand, the $\Delta\delta_{\text{init}}$ matches well with the corresponding analytical value calculated using (3.4) in the presence of virtual reactance, since the virtual reactance reshapes the reactance seen between the virtual back EMF and the PCC voltage of the VSM. This could be seen as one of the advantages of having virtual impedance for estimating the cycle-to-cycle load angle jump.

## 4.5 Impact of grid X/R ratio on voltage vector shift-based island detection method

Fig. 4.8 shows the pre-island power flows for the two cases of the X/R ratio. The entire net-load power of 0.3 p.u. is imported from the grid. Fig. 4.9 shows the impact of the high and low values of the grid X/R ratio on the VVS-based IDM for an islanding event. The cycle-to-cycle load angle jump as shown in Fig. 4.9 (d) is larger for a grid X/R ratio of 2 in comparison to an X/R ratio of 10. This is because for a grid X/R ratio of 2, the $Q_{\mathrm{vsm}}$ required to maintain the PCC voltage to 1 p.u. is 1.31 MVar, which is larger than that for a grid X/R ratio of 10. Fig. 4.9 (b) shows the difference in the values of $Q_{\mathrm{vsm}}$ for the two cases. This indicates that the grid impedance affects the initial reactive power output from the VSM. The reactive power change at the terminal of the VSM during the islanding event will affect the load angle jump of the VSM especially when the virtual impedance of the VSM has a low X/R ratio.

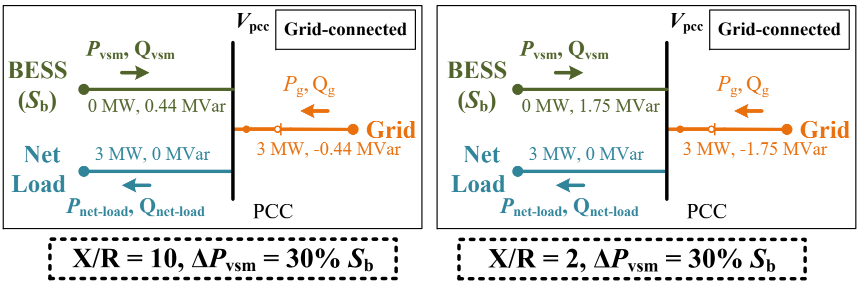


**Figure 4.8:** Power flows to analyze the impact of grid X/R ratio on VVS-based IDM

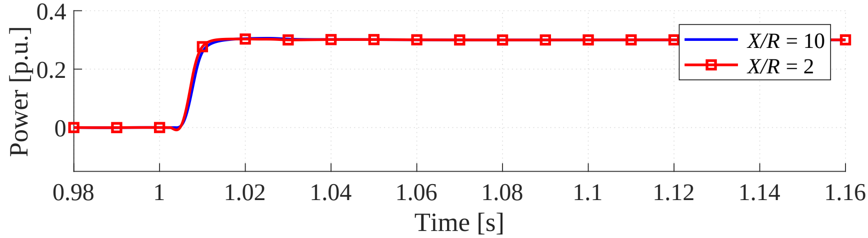


(a) Active power output from VSM

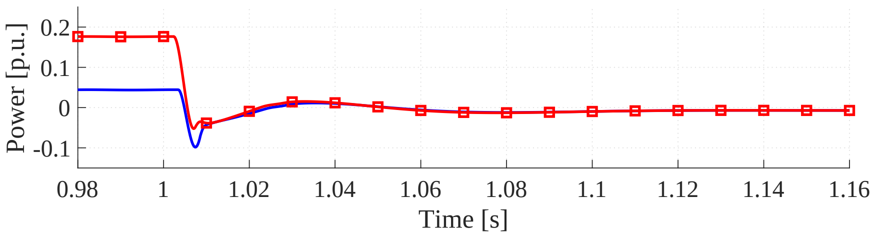


(b) Reactive power output from VSM

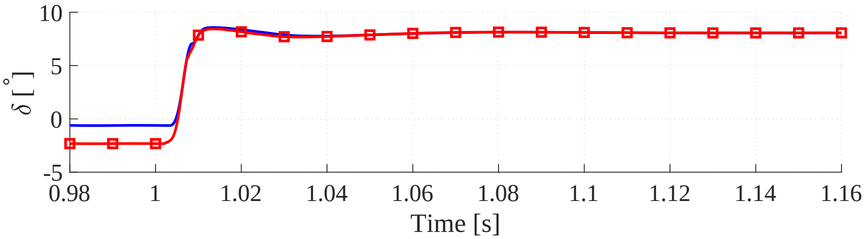


(c) PQ-based estimated load angle

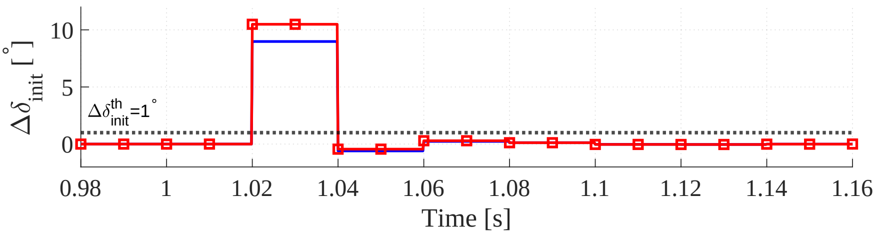


(d) Cycle-to-cycle load angle jump

**Figure 4.9:** Impact of grid X/R ratio on the composite VVS-based IDM for an islanding event. $\Delta P_{\mathrm{vsm}} = 30\%\ S_{\mathrm{b}}$, $H_{\mathrm{vsm}} = 3$ s, $K_{\mathrm{D}} = 89.40$ p.u., $\alpha_{\mathrm{f}} = 1.86$ rad/s.

## 4.6 Impact of VSM control on the island detection time of frequency-based island detection method

### 4.6.1 Impact of inertia constant

Fig. 4.10. shows the impact of virtual inertia constant $H_{\mathrm{vsm}}$ on island detection time by using $\Delta\theta_{\mathrm{r}}$-based IDM at different power imports from the main grid to the microgrid. In this case, the damping constant $K_{\mathrm{D}}$ and filter bandwidth $\alpha_{\mathrm{f}}$ are kept constant and equal to 89.40 p.u. and 1.86 rad/s, respectively. The simulation results match well with the analytical results obtained from (3.17). At a given import power, the island detection time becomes longer when the $H_{\mathrm{vsm}}$ of VSM increases because of a slower reduction in frequency. It is thus important to tune the $H_{\mathrm{vsm}}$ value by accounting for both the need of inertia support during the grid connected mode and the required speed of island detection. On the other hand, if a given $H_{\mathrm{vsm}}$ of VSM is required, one may adjust the threshold value for $\Delta\theta_{\mathrm{r}}$ to achieve a desired island detection time. However, the reduction in the threshold value may increase the risk of misdetection, and thus should be evaluated carefully. The analytical equation (3.17) provides the threshold values for the inertial support and island detection time desired by the operator and/or MG owner.

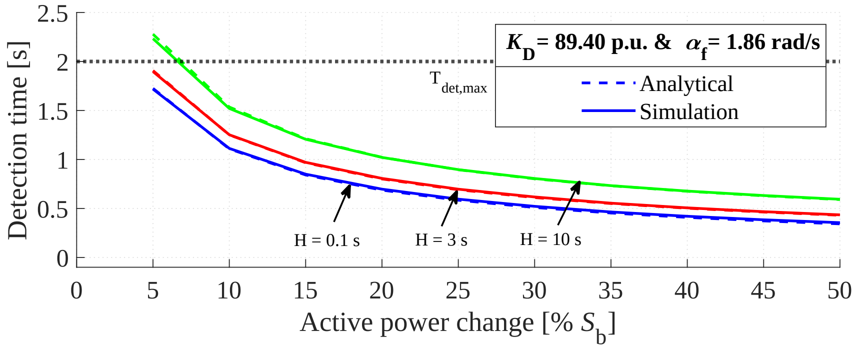


**Figure 4.10:** Detection time vs active power change for different values of $H_{\mathrm{vsm}}$

### 4.6.2 Impact of effective damping

The parameters $K_{\mathrm{D}}$ and $\alpha_{\mathrm{f}}$ affect the effective damping of the VSM. Fig. 4.11 shows the island detection time as a function of import power for three different values of $K_{\mathrm{D}}$. The simulation results also match well with the analytical results obtained from (3.17). As shown in the figure, it takes a longer time to detect the island as the damping constant increases. This is because the VSM frequency ramps down slower in the case of high-frequency damping. Thus, it takes a longer time for the rotor angle deviation $\Delta\theta_{\mathrm{r}}$ to reach its threshold of $\pm 45°$. Similarly, the island detection time becomes longer in case of a smaller filter bandwidth $\alpha_{\mathrm{f}}$, corresponding to a higher effective damping. A large damping constant is effective in damping the power oscillation. However, it will lead to a slower speed of island detection. Thus, the tuning of the effective damping should weigh between the need to damp power oscillation and the required speed of island detection. The base values of parameters $K_{\mathrm{D}}$ and $\alpha_{\mathrm{f}}$ are designed for a base inertia constant using the tuning approach proposed in [44]. For such tuned parameters, the speed of island detection can be adjusted by the selection of the threshold of the $\Delta\theta_{\mathrm{r}}$-based IDM.

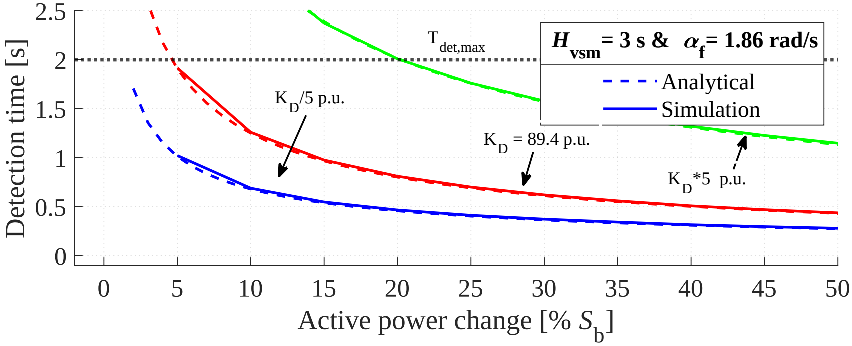


**Figure 4.11:** Detection time vs active power change for different values of $K_{\mathrm{D}}$

### 4.6.3 Impact of load type and electrical distance of the load

Fig. 4.12 shows the impact of load type and the electrical distance between the load and the BESS from the PCC on the island detection time for different power imports from the grid. Three cases are evaluated: a) constant impedance or constant power load connected to PCC, b) constant impedance load 15 km away from PCC, and c) constant power load 15 km away from PCC.

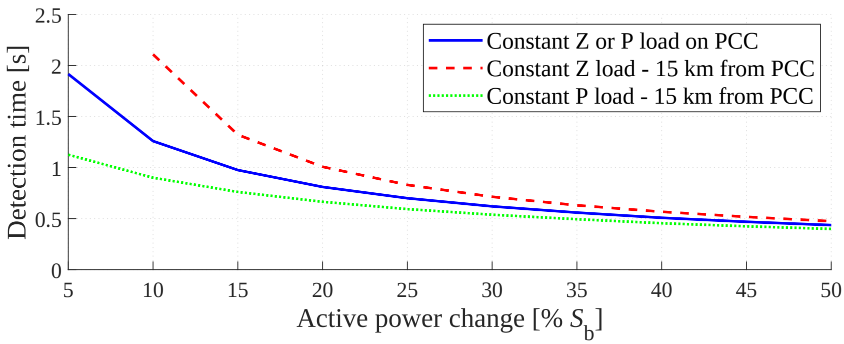


**Figure 4.12:** Island detection time vs. active power change for constant power and constant impedance load connected at PCC and 15 km away from PCC.

The BESS controls its PCC voltage to 1 p.u. As the load is connected further way from the PCC, the load voltage will be lower than the PCC voltage, which leads to a reduction in the load current and hence power due to load voltage dependence of the constant impedance load. As a result, the island detection time becomes longer for a load that is further away from the PCC where BESS is connected, as in case b) compared to case a). In contrast, in the case of a constant power load, the load power is independent of the change in the voltage. The active power change at PCC includes both the rated load power and the increased line losses. This increased active power change reduces the island detection time.

## 4.7 Risk of misdetection under grid disturbances

Three cases have been performed to evaluate the impact of the VSM controller on the risk of misdetection by using composite IDM under grid frequency variation and voltage angle jump. Fig. 4.13 shows the pre-disturbance power flow used to analyze the risk of misdetection. Before a grid disturbance occurs, 0.25 p.u. of active power is imported from the grid and 0.05 p.u. of active power is provided by the BESS for the net-load of 0.3 p.u.. The grid disturbance is applied t = 1 s.

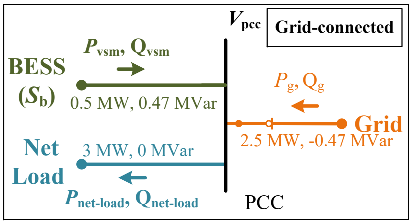


**Figure 4.13:** Power flows to analyze the risk of misdetection for grid frequency variation and grid voltage phase angle jump

The cases simulated are:

1. Base case: $H_{\text{vsm}} = 3$s, $K_{\text{D}} = 89.40$ p.u., and $\alpha_{\text{f}} = 1.86$ rad/s
2. Low H: $H_{\text{vsm}} = 0.1$ s, $K_{\text{D}} = 89.40$ p.u., and $\alpha_{\text{f}} = 1.86$ rad/s,
3. Low H and Low $K_{\text{D}}$: $H_{\text{vsm}} = 0.1$ s, $K_{\text{D}} = 17.88$ p.u., and $\alpha_{\text{f}} = 1.86$ rad/s.

The base case corresponds to a slower synchronization and large inertial support to the grid because of larger values of both $H_{\text{vsm}}$ and $K_{\text{D}}$. In the Low H case, the synchronization is also slow due to the high value of damping. The Low H and Low $K_{\text{D}}$ case provides the fastest synchronization speed among the three cases with the lowest value both in virtual inertia constant and effective damping.

### 4.7.1 Grid frequency variation

A grid frequency variation, as shown in the solid line in Fig. 4.14 (a), is simulated according to the frequency withstand capability requirement for generators specified by ENTSOE [48]. However, with addition of more and more IBRs more severe RoCoF than of generators can be expected.

The resulting VSM frequency for each of the three cases is also shown in Fig. 4.14 (a). If the VSM is designed to achieve fast grid synchronization like in Case 3, the resulting initial voltage angle jump caused by the grid frequency variation will be very small, which suppress the risk of misdetection. On the other hand, in Case 1 or Case 2, the synchronization between the VSM and the grid is slow as shown in Fig. 4.14 (a). As a result, the cycle-to-cycle load angle jump exceeds the threshold of 1° as shown in Fig. 4.14 (b). This will then activate the calculation of the rotor angle deviation $\Delta\theta_{\mathrm{r}}$, which reaches the threshold of 45° due to grid frequency variation as shown in Fig. 4.14 (c). Consequently, the grid frequency variation event is misdetected as an islanding event. One important reason to adopt the composite IDM is to use VVS-based IDM to distinguish the grid frequency variation event from an islanding event. However, this cannot be achieved if the synchronization loop of the VSM is too slow.

### 4.7.2 Grid voltage angle jump

Fig. 4.15 simulates another event where the grid voltage drops to 0.87 p.u. with an angle jump of $-35°$. Such a large grid angle jump will trigger the VVS-based IDM, which activates the calculation of rotor angle deviation $\Delta\theta_{\mathrm{r}}$. Compared to Case 1 and 2, Case 3 has lower inertia and damping, which leads to a faster change in VSM frequency. However, the VSM frequency in Case 3 is brought back to the pre-disturbance value faster because of a faster synchronization loop. Consequently, the $\Delta\theta_{\mathrm{r}}$ in Case 3 does not reach the threshold of $-45°$. In Case 2, the recovery of frequency is faster than that in Case 1 due to lower inertial power. However, the high damping power still slows down the recovery of the frequency, pushing $\Delta\theta_{\mathrm{r}}$ toward the threshold. This implies that a VSM with high inertial and damping power has a higher tendency to misdetect grid voltage angle jump as an islanding event. Hence to mitigate misdetection in case of grid voltage angle jump, a faster synchronization loop, corresponding to a low virtual inertia constant and damping, is desired.

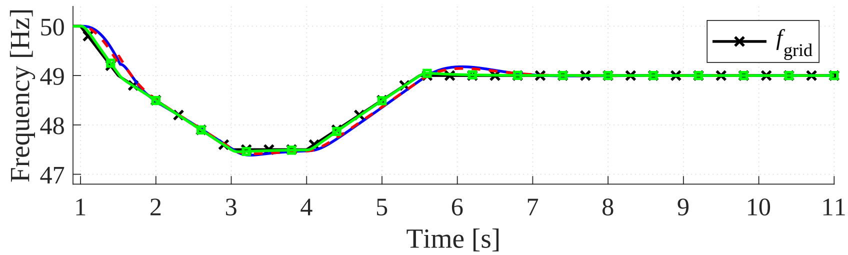


(a) Applied grid frequency profile and measured VSM frequency

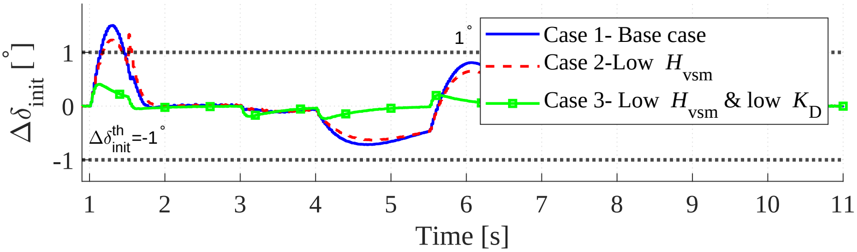


(b) Cycle-to-cycle load angle jump

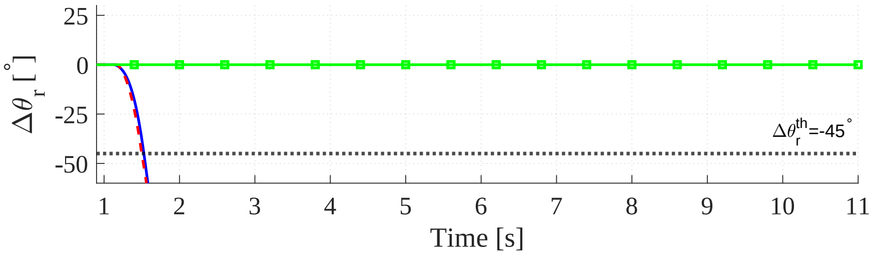


(c) Accumulated rotor angle change

**Figure 4.14:** Impact of grid frequency variation on the composite VVS-based island detection for a $\Delta P_{\text{vsm}} = 25\% S_{\text{b}}$. (Case 1- $H_{\text{vsm}} = 3$ s, $K_{\text{D}} = 89.40$ p.u., $\alpha_{\text{f}} = 1.86$ rad/s. Case 2- $H_{\text{vsm}} = 0.1$ s, $K_{\text{D}} = 89.40$ p.u., $\alpha_{\text{f}} = 1.86$ rad/s. Case 3- $H_{\text{vsm}} = 0.1$ s, $K_{\text{D}} = 17.88$ p.u., $\alpha_{\text{f}} = 1.86$ rad/s.)

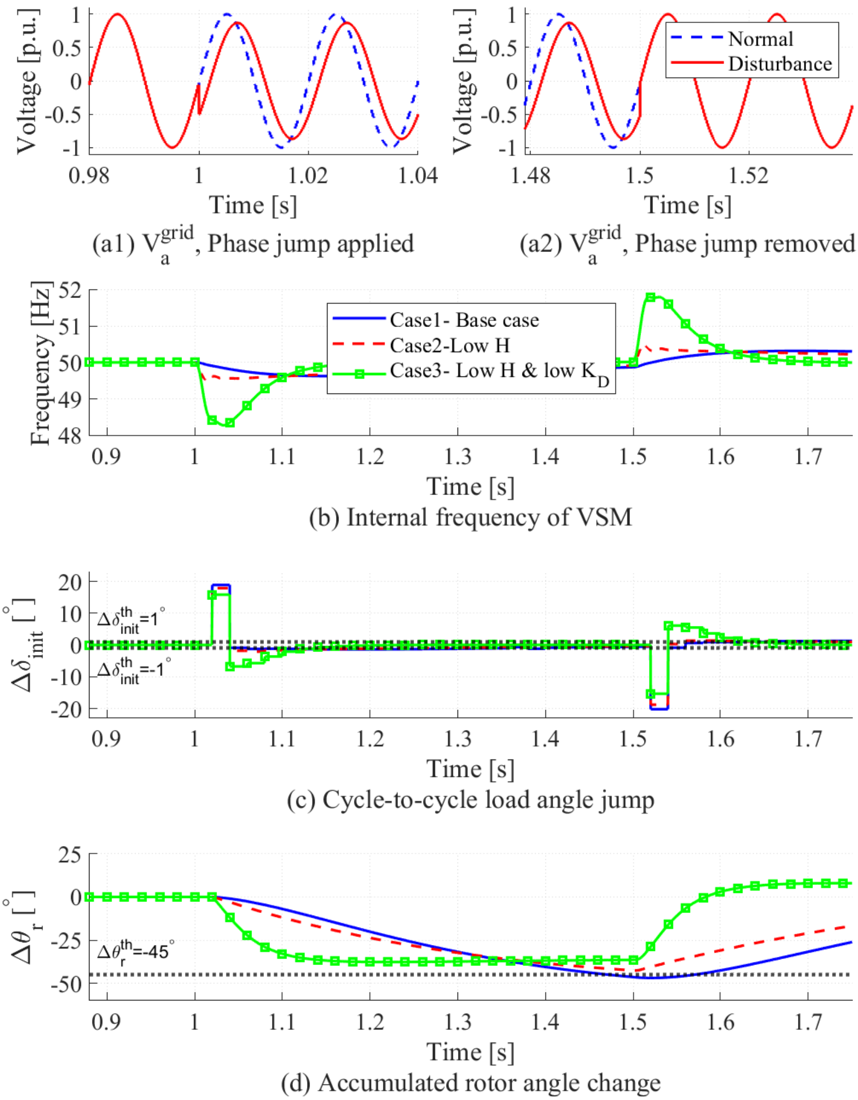


**Figure 4.15:** Impact of combined voltage dip and phase jump on the composite VVS-based island detection $\Delta P_{\mathrm{vsm}} = 25\% S_{\mathrm{b}}$. (Case 1- $H_{\mathrm{vsm}} = 3$ s, $K_{\mathrm{D}} = 89.40$ p.u., $\alpha_{\mathrm{f}} = 1.86$ rad/s. Case 2- $H_{\mathrm{vsm}} = 0.1$ s, $K_{\mathrm{D}} = 89.40$ p.u., $\alpha_{\mathrm{f}} = 1.86$ rad/s. Case 3- $H_{\mathrm{vsm}} = 0.1$ s, $K_{\mathrm{D}} = 17.88$ p.u., $\alpha_{\mathrm{f}} = 1.86$ rad/s.)

## 4.8 Summary

A medium voltage microgrid case study with VSM-based GFM controller is simulated in MATLAB/Simulink. The impact of different controller parameters on the VVS- and frequency-based passive IDM is analyzed for an islanding event as well as for grid disturbances. The following are the main conclusions from the analyzed results:

- The load angle estimated using the proposed PQ-based method shows better performance than the dq-based method as the former is less affected by the electrical transients within each electrical cycle.
- The presence of virtual impedance reshapes the impedance seen between the virtual back EMF and the PCC voltage. This reduces the risk of an increased NDZ caused by the estimation error of physical filter parameters.
- The low value of inertia and damping corresponding to a fast synchronization loop reduces the island detection time. Furthermore, it also reduces the risk of misdetection when facing a large variation in the grid frequency or angle jump in the grid voltage.
- However, during grid connected conditions, a relatively large inertial support is desired in case of a high RoCoF event in the grid. Furthermore, a low value of damping can cause high power oscillations between the VSM and the grid when subjected to small disturbances. Thus, there is a trade-off in tuning the VSM parameters between the need of inertial support and damping during grid-connected conditions and the need of a reliable and fast island detection during an islanding event.

# CHAPTER 5

# Experimental Verification

## 5.1 Description of experimental setup

Fig. 5.1 depicts the implemented laboratory setup for verifying the performance of the composite island detection method in an MG. The MG is powered by an ac power amplifier, which emulates the electrical behavior of a VSM .

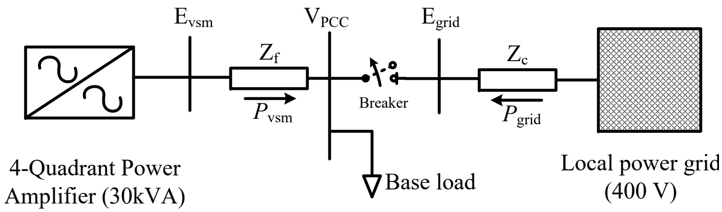


**Figure 5.1:** Lab setup for evaluating the performance of composite island detection method in an MG powered by a grid-forming inverter

The 30 kVA ($S_{\mathrm{ACS}}$) power amplifier is a 4-quadrant ACS power amplifier from Regatron. The controller for VSM is implemented in dSPACE

Microlabbox, which sends the reference voltage signals to the ACS running in amplifier mode. The $Z_\mathrm{f}$ represents the filter impedance of the VSC, i.e. $0.05 + j0.95\ \Omega$. The local 400 V grid is highly resistive. In order to reflect better the characteristics of a medium voltage distribution grid, an impedance of $Z_\mathrm{c} = 0.7 + j0.4750\ \Omega$ is connected between the ACS and the 400 V grid. This impedance reflects the X/R ratio of a 12 kV 150 mm$^2$ underground cable [49]. The short circuit ratio between the grid at PCC and the ACS is 2.1. A switchable resistive load rated 9 kW (0.3 p.u.) is connected to the PCC, with power steps of 0, 4.5 kW, and 9 kW. A breaker is used to connect or disconnect the grid for creating an islanding event. In this case, the ACS has a higher rating than the 9 kW load which is typically not the case in reality. However, this does not affect the analyses and conclusions of the results. This is because the purpose here is to vary the exchange power between the MG and the main grid for evaluating the performance of the island detection methods, especially when the exchange power is relatively small concerning the rating of ACS. The controller parameters of the VSM are selected similarly to the simulation model stated otherwise.

## 5.2 PQ-based vs dq-based load angle estimation for voltage vector shift-based island detection method

Fig. 5.2 shows the power flow in the MG laboratory setup before and after the disconnection of the main grid. Before the islanding event, the MG imports 0.833 p.u. of active power from the main grid. Fig. 5.3 shows the corresponding measurement of the VSM load angle estimated using the dq-based and the proposed PQ-based method during an islanding event. It is observed that the load angle estimated using the PQ-based method (blue dashed curve) contains not only fewer electrical transients within an electrical cycle, but also fewer harmonics, as compared to the dq-based method (red curve). The three-phase voltage in the local grid contains $5^{\mathrm{th}}$-order harmonic component, which becomes the $6^{\mathrm{th}}$-order harmonic in the synchronous dq coordinate. With no or insufficient filtering of the grid voltage, the harmonic components are seen as ac components by the integrator in the PLL. This may result in an amplified harmonic component in the estimated load angle as shown in the solid red curve in 5.3. However, the 6$^{th}$-order harmonic content is almost unobservable in the PQ-based method, because the method involves no integral action in estimation.

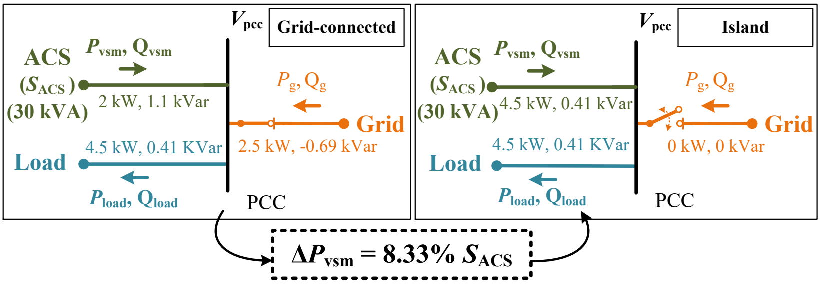


**Figure 5.2:** Power flow for MG lab setup to analyze the PQ-based vs dq-based load angle estimation before and after an islanding event

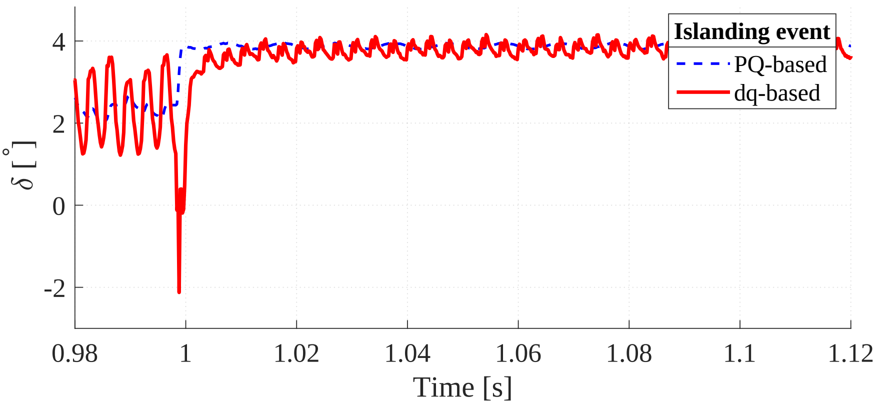


**Figure 5.3:** PQ-based vs dq-based load angle estimation for VVS-bsed island detection of MG laboratory setup for $\Delta P_{vsm} = 8.33\% S_{ACS}$ during an islanding event

Fig. 5.4 shows the power flow in the MG laboratory setup before and after a load switching event. The load is switched from 0 to 4.5 kW (0.15 p.u). Fig. 5.5 shows the corresponding load angle of the VSM using the dq-based and the proposed PQ-based estimation method. Similar phenomena as in the islanding event are observed, where the electrical transients in the dq-based method are clearly observable, and the PQ-based method provides a much better estimation of load angle at the fundamental frequency with much less harmonic distortion.

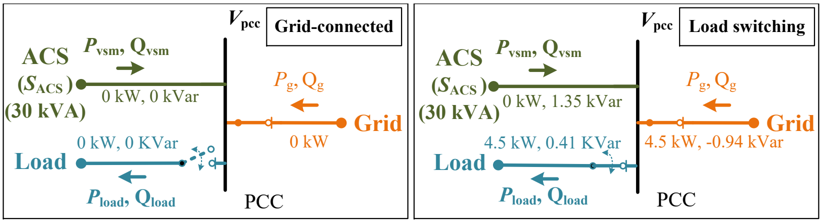


**Figure 5.4:** Power flow for MG laboratory setup to analyze the PQ-based vs dq-based load angle estimation in case of load switching

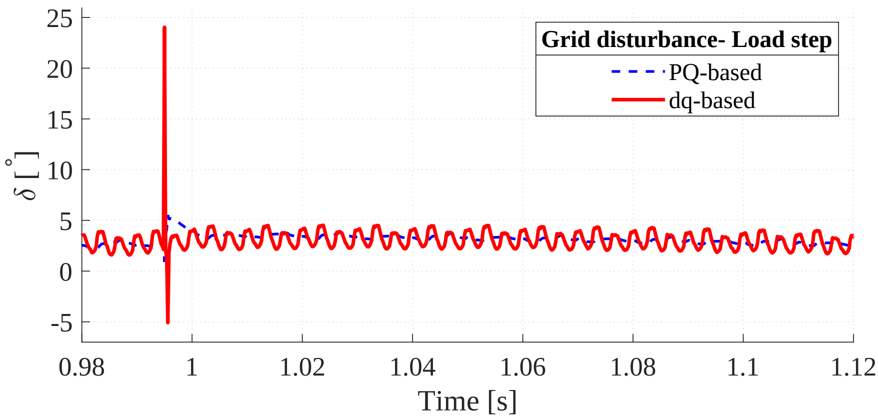


**Figure 5.5:** PQ-based vs dq-based load angle estimation for VVS-based island detection of an MG laboratory setup for $\Delta P_{vsm} = 15\% S_{ACS}$: load switching

## 5.3 Impact of virtual impedance on non-detection zone of voltage vector shift-based island detection method

Fig. 5.2 illustrates the power flows before and after an islanding event. Fig. 5.6 shows the corresponding results of active power output from the VSM, the load angle of the VSM, and the cycle-to-cycle change of the load angle during an islanding event. Two cases with two different values of virtual impedance are tested, i.e. $Z_{\mathrm{v}}$ =0.015+j0.15 p.u. and $Z_{\mathrm{v}}$ = 0.25+j0.5 p.u. Although both $R_{\mathrm{v}}$ and $X_{\mathrm{v}}$ are changed in the experiment, it is mainly the virtual reactance that affects the area of the NDZ. According to the analytical expression in (3.6) and simulation results in Fig. 3.2, the NDZ widens as the virtual reactance reduces. This is verified in the laboratory test as shown in Fig. 5.6 (b) and (c), where the red-dashed case with a lower virtual reactance failed to detect the islanding event, even though the change of the active power experienced by the VSM is more or less the same between the two cases according to Fig. 5.6 (a).

## 5.4 Impact of VSM control on the island detection time of the frequency-based island detection method

Three different cases as shown in Table 5.1 are performed in the laboratory to demonstrate the impact of the virtual inertia constant ($H_{\mathrm{vsm}}$) and the effective damping on the island detection time. Two values of active power change 30% (9 kW) and 15% (4.5 kW) are selected for the experiment. The detection time obtained from the laboratory results matches closely with the analytical values obtained from (3.17). This indicates that, when using rotor angle deviation $\Delta\theta_{\mathrm{r}}$-based IDM, the analytical expression developed in (3.17) can be directly used to evaluate the island detection time for a given virtual inertia constant and damping constant without resorting to time domain simulation. The same conclusion can be draw when the frequency deviation $\Delta f$-based IDM is used.

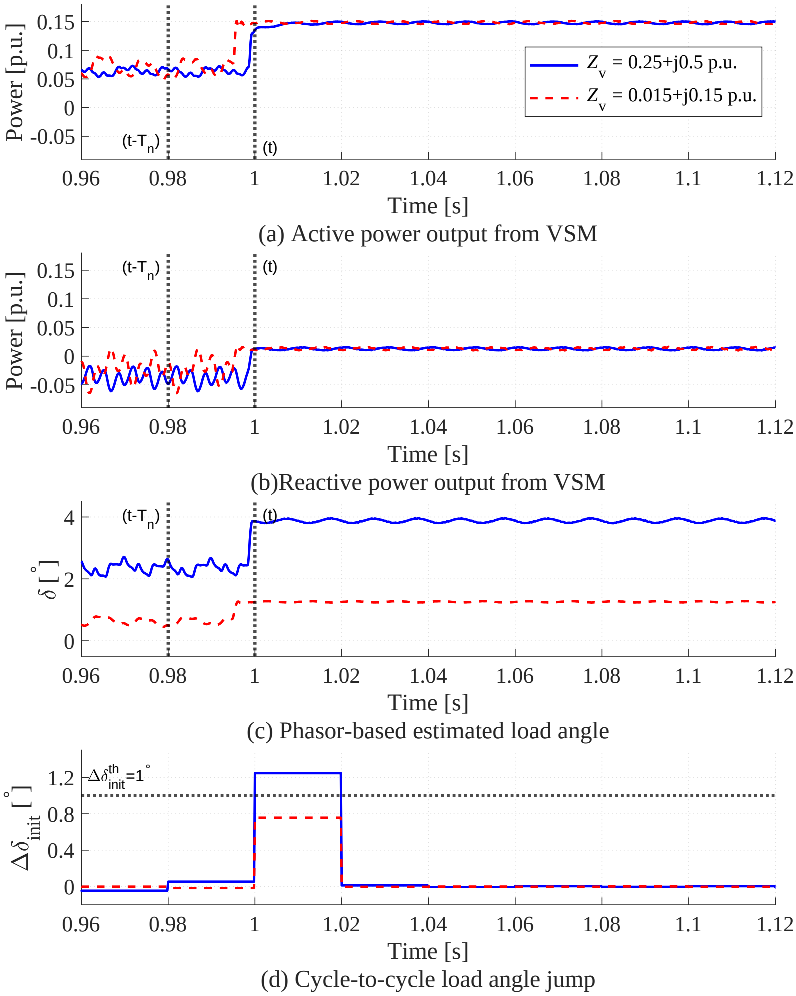


**Figure 5.6:** Island case: Impact of change of virtual impedance on the non-detection zone of VVS-based island detection for $\Delta P_{\mathrm{vsm}} = 8.33\%\ S_{\mathrm{ACS}}$

**Table 5.1:** Experimental tests of island detection time using composite IDM at different settings of virtual inertia constant and damping

| Cases | $\Delta P(\%S_{\mathrm{ACS}})$ | $T_{\mathrm{det}}$ (s) | |
|---|---|---|---|
| | | **Analytical** | **Laboratory results** |
| $H_{\mathrm{vsm}} = 3$ s, $K_{\mathrm{D}} = 89.4$ p.u. | 30% | 0.61 | 0.61 |
| | 15% | 0.97 | 0.96 |
| $\boldsymbol{H}_{\mathbf{vsm}}\mathbf{= 0.1}$ s, $K_{\mathrm{D}} = 89.4$ p.u. | 30% | 0.51 | 0.51 |
| | 15% | 0.84 | 0.85 |
| $H_{\mathrm{vsm}} = 3$ s, $\boldsymbol{K}_{\mathbf{D}}\mathbf{= 89.4/5}$ p.u. | 30% | 0.36 | 0.37 |
| | 15% | 0.54 | 0.51 |

# 5.5 Risk of misdetection under grid disturbances

## 5.5.1 Load switching

Fig. 5.4 shows the power flow before and after the resistive load is switched from 0 to 4.5 kW (15% $S_{\mathrm{ACS}}$).

Fig. 5.7 shows the corresponding dynamic response during the load switching event, in terms of active power from the VSM to the grid, load angle from the VSM and the cycle-to-cycle load angle jump for two different values of virtual impedances ($Z_{\mathrm{v}}$). For the given base value of $Z_{\mathrm{v}} = 0.25+\mathrm{j}0.5$ p.u., the change in the load angle is sufficiently large to increase the cycle-to-cycle load angle jump above the threshold of 1°. This leads to a misdetection of the load switching as an islanding event. However, if a low $Z_{\mathrm{v}} = 0.015+\mathrm{j}0.15$ p.u. is selected, the cycle-to-cycle load angle jump is small and the misdetection can be avoided. This is because the change in the load angle is largely dictated by the active power output from the VSM and the value of virtual reactance $X_{\mathrm{v}}$. According to (3.2), for a given active power change, a larger value of $X_{\mathrm{v}}$ causes a larger load angle change, which may lead to a misdetection of load switching as an islanding event. Although a low $Z_{\mathrm{v}}$ will avoid the misdetection in the case of grid disturbance such as load switching, it will increase the area of a non-detection zone in case of an actual island as observed in Fig. 5.6. Typically, a high value of virtual impedance is selected for grid connected operation to reduce the impact of grid impedance on the design of voltage controller. Thus increasing the probability of misdetection for a grid disturbance. One way to avoid misdetection is to increase the threshold of the VVS-based method. But, this will decrease the sensitivity of the method to

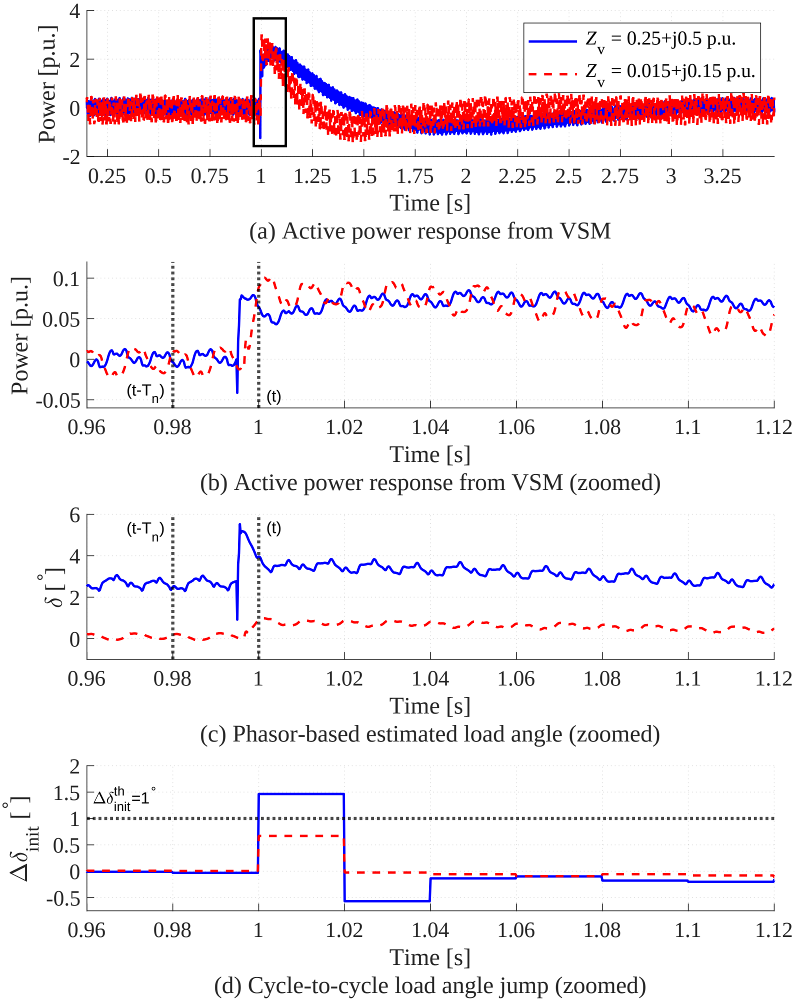


**Figure 5.7:** Misdetection by VVS-based island detection during a load switching event for $\Delta P_{\mathrm{vsm}} = 15\% S_{\mathrm{ACS}}$ and two different values of virtual impedance

an actual island thereby increasing the NDZ.

### 5.5.2 Estimation of rotor angle deviation under grid frequency variation

For a grid disturbance of load switching or voltage angle jump VVS-based method will trigger the estimation of $\Delta\theta_{\mathrm{r}}$. From Fig. 3.4 (b), it can be observed that the $\Delta\theta_{\mathrm{r}}$ is calculated using the deviation of VSM frequency $\omega_{\mathrm{vsm}}(k)$ from $\omega_{0,\mathrm{vsm}}(k)$, where $\omega_{0,\mathrm{vsm}}(k)$ is VSM frequency $\omega_{\mathrm{vsm}}(k)$ averaged over past five cycles at the instant of triggering. In reality, the grid frequency is not constant and has small but continuous deviation from the base frequency of 50 Hz. Hence, for a grid connected case, the BESS frequency exhibits the same deviations as it follows the grid frequency. This causes the $\Delta\theta_{\mathrm{r}}$ to continuously accumulate. Over time this may lead to the misdetection of the grid disturbances as an islanding event. Fig. 5.8 (a) shows the measured frequency of the grid using a PLL (red) and BESS internal frequency (green with markers). The $\Delta\theta_{\mathrm{r}}$ calculated using the $f_{\mathrm{pre-disturbance}}$ value is shown in Fig. 5.8 (b). The $\Delta\theta_{\mathrm{r}}$ continues to accumulate and reaches the threshold of -45° around 11.5 s.

One way to tackle this problem is that for the composite IDM, replace the $\Delta\theta_{\mathrm{r}}$-based by the $\Delta f$- based method. The threshold value for the $\Delta f$- based method should be sufficiently large to reduce misdetection in case of grid frequency variation, but not too large to activate the over- or under-frequency relay that will disconnect the local generators and/or loads. Another approach could be to use the remote measurement of grid frequency and track the angle separation between the virtual back EMF angle of the VSM and the grid angle at a remote measurement point. However, the method will no longer be a 'local passive' IDM and relies on a communication medium to receive the remote measurement. Further analysis on a more effective passive IDM is required in the future.

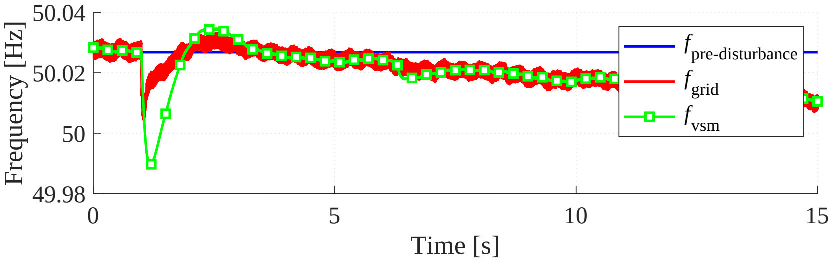


(a) Measured grid frequency and internal VSM frequency

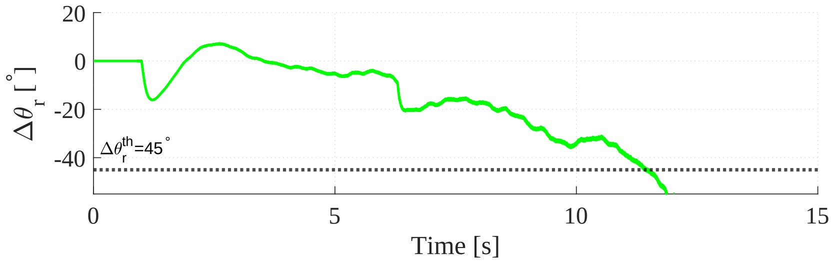


(b) Accumulated rotor angle change

**Figure 5.8:** Impact of the use of an internal VSM frequency on the estimation of $\Delta\theta_r$ after a load switching event

## 5.6 Summary

The proposed PQ-based load angle estimation method and the composite passive IDM are tested in an MG setup in the laboratory. The VSM-based GFM control is implemented in the Regatron ACS power amplifier, which emulates the electrical behavior of a BESS. The conclusions are summarized as follows:

- The laboratory experiment confirms the observation from the simulation that the PQ-based method for load angle estimation is better than the dq-based estimation method. The PQ-based method contains fewer harmonics and electrical transients within an electrical cycle both during the actual islanding event and during a grid connected load switching event.
- The area of a non-detection zone (NDZ) for the selected VVS-based passive IDM is affected principally by the virtual reactance. The area of NDZ is increased for the decrease in the virtual reactance value as observed in laboratory experiments, which is in line with the conclusions drawn from the simulation results and the theoretical analysis.
- The island detection time values obtained in the lab experiment for different cases verify the analytical expression of island detection time as a function of VSM-based GFM controller parameters.
- For a grid connected load switching event, a small value of virtual reactance is preferred to reduce the risk of misdetection. However, a small virtual reactance increases the NDZ of the VVS-based IDM. A trade-off in the selection of the virtual reactance is thus needed.

# CHAPTER 6

# Conclusions and Future Work

## 6.1 Conclusions

This work has identified key factors that influence the performance of passive island detection methods in an MG powered by a grid forming IBR using VSM control. The key factors are related to the parameter settings of the VSM controller, including virtual impedance, virtual inertia constant, effective damping, and voltage controller integral gain. Table 6.1 summarizes how these controller parameters affect the performance of the analyzed passive IDMs. The following conclusions can be derived from the simulation and experimental results obtained in the thesis:

- To achieve a small area of $\Delta P - \Delta Q$ NDZ of a VVS-based IDM, a relatively large virtual reactance is desired.
- The slope of the $\Delta P - \Delta Q$ NDZ increases as the R/X ratio of the virtual impedance increases.
- A fast synchronization loop, with a low value of inertia constant and damping power, reduces not only the island detection time but also the

risk of misdetection when facing a large variation in the grid frequency or angle jump in the grid voltage.

- A low inertia constant implies a low inertial contribution during the grid-connected condition and a high RoCoF for the VSM when subject to a large active power disturbance.
- Low damping also leads to a high power oscillation between the VSM and the grid under a small disturbance in the grid.
- Overall, when tuning the VSM control parameters, one needs to weigh the importance between the need of the inertial support and damping during grid-connected conditions and the need of a reliable and fast island detection method.
- A slow voltage controller overestimates the cycle-to-cycle load angle jump creating a possibility of mis-detection of grid disturbances as an islanding event
- The proposed PQ-based method gives a more stable performance than the dq-based method in estimating the cycle-to-cycle load angle jump for the VVS-based IDM. This is because the PQ-based method is less sensitive to the electrical transients within each electrical cycle.

## 6.2 Future Work

The thesis has focused on a simple MG with a single grid forming inverter to analyze the impact of the VSM-based grid forming controller parameters on the passive island detection. In reality, the MG may consist of both grid following and grid forming inverters along with the traditional synchronous generators. It will be interesting to extend the analysis presented in this thesis to a MG comprising of both grid forming and grid following inverters. Moreover, with the increasing inclination towards grid-forming inverter, stability case studies for multiple grid forming units, especially during coordination between frequency controller and load shedding will also be interesting. Furthermore, the thesis has focused on passive island detection methods, whereas active detection methods can be further explored to reduce the non-detection

**Table 6.1:** Summary of VSM controller parameters that affect the performance of analyzed passive island detection methods

| VSM based Grid forming controller parameter | During Grid-Connected Mode | | | | For Island Detection | | |
|---|---|---|---|---|---|---|---|
| | Grid support function | Mitigate misdetection | | | Fast Island detection | Flat slope of $\Delta P$ - $\Delta Q$ NDZ | Small area of $\Delta P$ - $\Delta Q$ NDZ |
| | | Grid frequency variation | Grid voltage phase angle jump | Load switching | | | |
| | | VVS-based or composite IDM | | | $\Delta f$-based or composite IDM | VVS-based IDM | |
| Virtual reactance, Xv | High- less sensitive to grid impedance for voltage controller design | Low | N/A | Low | N/A | High* | High |
| Rv/Xv | High- to damp the dc component of current | High | N/A | Low | N/A | Low | Low** |
| Inertial constant, $H_{\mathrm{vsm}}$ | High- inertial support | Low | Low | Low | Low | N/A | N/A |
| Damping, $K_{\mathrm{D}}$ or $1/\alpha_{\mathrm{f}}$ | High- power oscillation damping | Low | Low | Low | Low | N/A | N/A |
| Voltage controller integral gain $K_{\mathrm{i,vr}}$ | Moderate- stable voltage control | High | N/A | High | N/A | N/A | Low |

* - High value of virtual reactance is due to the low value requirement of $R_{\mathrm{v}}/X_{\mathrm{v}}$
** - Low value of $R_{\mathrm{v}}/X_{\mathrm{v}}$ is due to the high value of high value of virtual reactance

zone and to improve the island detection time. Moreover, the benefits of individual MGs such as reliability improvement and ancillary service support can be enhanced by connecting the two adjacent MGs together to form a nested microgrid (NMG)[7]. Within NMG each MG may have its own IDM and its respective threshold settings. Because of the different thresholds, one MG may detect the island sooner and update the protection settings accordingly while the other operates as grid connected. This may lead to unnecessary tripping and disconnection of sections of the MG. Thus the analysis of the impact of IDMs with different island detection criteria for different MGs on protection coordination, voltage and frequency stability of the NMG could be a challenging task. Another topic of future investigation is to use MG with blackstart capability to assist the blackstart of another MG lacking the blackstart capability.

# References


[1] "2050 long-term strategy." (2022), [Online]. Available: https://climate.ec.europa.eu/eu-action/climate-strategies-targets/2050-long-term-strategy_en#documentation) (visited on 09/26/2022).

[2] H. Pörtner, D. Roberts, H. Adams, *et al.*, *Climate change 2022: impacts, adaptation and vulnerability*, English. IPCC, 2022.

[3] "Renewable energy." (2021), [Online]. Available: https://www.eea.europa.eu/themes/energy/renewable-energy (visited on 09/26/2022).

[4] "Cross-party policy agreement – 100% renewable by 2040, but no cut-off for nuclear." (2016), [Online]. Available: https://rb.gy/xc7kks (visited on 09/26/2022).

[5] R. H. Lasseter, "Microgrids and distributed generation," *Journal of Energy Engineering*, vol. 133, no. 3, pp. 144–149, 2007.

[6] J. Leader and R. Tucker, "Microgrid- the role of microgrids in the regulatory compact," Smart Electric Power Alliance, 2019, pp. 1–16.

[7] S. Inamdar, R. Mohanty, P. Chen, R. Majumder, and M. Bongiorno, "On benefits and challenges of nested microgrids," in *2019 IEEE PES Asia-Pacific Power and Energy Engineering Conference (APPEEC)*, 2019, pp. 1–6.

[8] "We are renewing SIMRIS." (2022), [Online]. Available: https://www.eon.se/en_US/om-e-on/local-energy-systems/we-are-renewing-simris (visited on 09/26/2022).

[9] "Ö-drift Arholma." (), [Online]. Available: `https://www.vattenfalleldistribution.se/var-verksamhet/innovation/arholma/` (visited on 09/26/2022).

[10] O. N. Hurtig, M. Arvidsson, M. Hessman, *et al.*, "Drivers and barriers to deploy microgrid in sweden," in *2022 IEEE PES Innovative Smart Grid Technologies Europe (ISGT Europe)*, 2022, pp. 1–6.

[11] "Miljö- och energidepartementet. Ellag (1997:857), Chapter 3, Section 9a.," Ministry of Infrastructure RSED E, 2022.

[12] R. Mohanty, P. Chen, and L. A. Tuan, "Protection of converter dominated mv microgrid using changes in current's phase angle," *IET Generation, Transmission & Distribution*, vol. 16, no. 4, pp. 656–668, 2022.

[13] M. S. Kim, R. Haider, G. J. Cho, C. H. Kim, C. Y. Won, and J. S. Chai, *Comprehensive review of islanding detection methods for distributed generation systems*, Mar. 2019.

[14] M. Ropp, M. Begovic, A. Rohatgi, G. Kern, R. Bonn, and S. Gonzalez, "Determining the relative effectiveness of islanding detection methods using phase criteria and nondetection zones," *IEEE Transactions on Energy Conversion*, vol. 15, no. 3, pp. 290–296, 2000.

[15] C. Li, C. Cao, Y. Cao, Y. Kuang, L. Zeng, and B. Fang, "A review of islanding detection methods for microgrid," *Renewable and Sustainable Energy Reviews*, vol. 35, pp. 211–220, 2014, ISSN: 1364-0321.

[16] S. Dutta, M. J. B. Reddy, D. K. Mohanta, M. S. Kushwah, and P. K. Sadhu, "$\mu$PMU-based intelligent island detection – the first crucial step toward enhancing grid resilience with mg," *IET Smart Grid*, vol. 3, no. 2, pp. 162–173, 2020.

[17] "Requirements for grid connection applicable to all generators," ENTSO-E, IMPLEMENTATION GUIDELINE FOR NETWORK CODE, 2013.

[18] O. Raipala, A. Mäkinen, S. Repo, and P. Järventausta, "An anti-islanding protection method based on reactive power injection and rocof," *IEEE Transactions on Power Delivery*, vol. 32, no. 1, pp. 401–410, 2017.

[19] "Evaluation of multi-inverter anti-islanding with grid support and ride-through and investigation of island detection alternatives," Sandia National Lab, Albuquer-que, NM, USA, 2019.

[20] A. Hoke, A. Nelson, B. Miller, S. Chakraborty, F. Bell, and M. M. Solarcity, "Experimental evaluation of pv inverter anti-islanding with grid support functions in multi-inverter island scenarios," National Renewable Energy Laboratory, Golden, CO, USA, 2016.

[21] H. Laaksonen, "Reliable islanding detection with active mv network management," CIRED Workshop, Jun. 2014.

[22] M. Karimi, M. Farshad, Q. Hong, H. Laaksonen, and K. Kauhaniemi, "An islanding detection technique for inverter-based distributed generation in microgrids," *Energies*, vol. 14, 1 Jan. 2021, ISSN: 19961073.

[23] W. Freitas, W. Xu, C. M. Affonso, and Z. Huang, "Comparative analysis between rocof and vector surge relays for distributed generation applications," *IEEE Transactions on Power Delivery*, vol. 20, pp. 1315–1324, 2 II Apr. 2005, ISSN: 08858977.

[24] W. Freitas, Z. Huang, and W. Xu, "A practical method for assessing the effectiveness of vector surge relays for distributed generation applications," *IEEE Transactions on Power Delivery*, vol. 20, pp. 57–63, 1 Jan. 2005, ISSN: 08858977.

[25] J. Xing and L. Mu, "A new passive islanding detection solution based on accumulated phase angle drift," *Applied Sciences (Switzerland)*, vol. 8, 8 Aug. 2018, ISSN: 20763417.

[26] S. Liu, S. Zhuang, Q. Xu, and J. Xiao, "Improved voltage shift islanding detection method for multi-inverter grid-connected photovoltaic systems," *IET Generation, Transmission and Distribution*, vol. 10, pp. 3163–3169, 13 Oct. 2016, ISSN: 17518687.

[27] C. Bright, "Corocof: Comparison of rate of change of frequency protection. a solution to the detection of loss of mains," in *2001 Seventh International Conference on Developments in Power System Protection (IEE)*, 2001, pp. 70–73.

[28] W. El-Khattam, A. Yazdani, T. S. Sidhu, and R. Seethapathy, "Investigation of the local passive anti-islanding scheme in a distribution system embedding a pmsg-based wind farm," *IEEE Transactions on Power Delivery*, vol. 26, pp. 42–52, 1 Jan. 2011, ISSN: 08858977.

[29] S. Salman, D. King, and G. Weller, "New loss of mains detection algorithm for embedded generation using rate of change of voltage and changes in power factors," in *2001 Seventh International Conference on Developments in Power System Protection (IEE)*, 2001, pp. 82–85.

[30] J. C. Vieira, W. Freitas, W. Xu, and A. Morelato, "An investigation on the nondetection zones of synchronous distributed generation anti-islanding protection," *IEEE Transactions on Power Delivery*, vol. 23, pp. 593–600, 2 Apr. 2008, ISSN: 08858977.

[31] S. A. Saleh, A. S. Aljankawey, R. Meng, J. Meng, L. Chang, and C. P. Diduch, "Apparent power-based anti-islanding protection for distributed cogeneration systems," *IEEE Transactions on Industry Applications*, vol. 52, pp. 83–98, 1 Jan. 2016, ISSN: 00939994.

[32] J. Muñoz-Cruzado-Alba, J. Villegas-Núñez, J. A. Vite-Frías, J. M. Carrasco-Solís, and E. Galván-Díez, "New low-distortion q-f droop plus correlation anti-islanding detection method for power converters in distributed generation systems," *IEEE Transactions on Industrial Electronics*, vol. 62, pp. 5072–5081, 8 Aug. 2015, ISSN: 02780046.

[33] H. R. Baghaee, D. Mlakic, S. Nikolovski, and T. Dragicevic, "Anti-islanding protection of pv-based microgrids consisting of phevs using svms," *IEEE Transactions on Smart Grid*, vol. 11, pp. 483–500, 1 Jan. 2020, ISSN: 19493061.

[34] Y. Lin, J. H. Eto, B. B. Johnson, *et al.*, "Research roadmap on grid-forming inverters," Golden, CO: National Renewable Energy Laboratory, NREL/TP-5D00-73476.

[35] R. Rosso, X. Wang, M. Liserre, X. Lu, and S. Engelken, "Grid-forming converters: Control approaches, grid-synchronization, and future trends—a review," *IEEE Open Journal of Industry Applications*, vol. 2, pp. 93–109, Apr. 2021.

[36] D. B. Rathnayake, M. Akrami, C. Phurailatpam, *et al.*, "Grid forming inverter modeling, control, and applications," *IEEE Access*, vol. 9, pp. 114 781–114 807, 2021, ISSN: 21693536.

[37] "Grid-forming technology in energy systems integration," Energy System Integration Group's High Share of Inverter-Based Generation Task Force, 2022.

[38] P. Christensen, G. K. Andersen, M. Seidel, *et al.*, "High penetration of power electronic interfaced power sources and the potential contribution of grid forming converters," ENTSO-E, 2020.

[39] T. Liu, X. Wang, F. Liu, K. Xin, and Y. Liu, "Islanding detection of grid-forming inverters: Mechanism, methods, and challenges," *IEEE Electrification Magazine*, vol. 10, no. 1, pp. 30–38, 2022.

[40] "Conformity assessment–ieee 1547–interconnection and interoperability of distributed energy resources (ders) with associated electric power systems (epss) interfaces," *IEEE/ICAP Conformity Assessment–IEEE 1547*, pp. 1–18, 2019.

[41] O. Samuelsson and N. Strath, "Islanding detection and connection requirements," in *2007 IEEE Power Engineering Society General Meeting*, 2007, pp. 1–6.

[42] "Frequency measurement requirements and usage," ENTSO-E, RGCE System Protection and Dynamics Sub Group, 2018.

[43] L. Zhang, L. Harnefors, and H. P. Nee, "Power-synchronization control of grid-connected voltage-source converters," *IEEE Transactions on Power Systems*, vol. 25, pp. 809–820, 2 May 2010, ISSN: 08858950.

[44] A. Narula, M. Bongiorno, M. Beza, and P. Chen, "Tuning and evaluation of grid-forming converters for grid-support," in *2021 23rd European Conference on Power Electronics and Applications (EPE'21 ECCE Europe)*, 2021, P.1–P.10.

[45] L. Harnefors, M. Hinkkanen, U. Riaz, F. M. Rahman, and L. Zhang, "Robust analytic design of power-synchronization control," *IEEE Transactions on Industrial Electronics*, vol. 66, pp. 5810–5819, 8 Aug. 2019, ISSN: 02780046.

[46] "Three-phase dynamic load." (2022), [Online]. Available: `https://se.mathworks.com/help/sps/powersys/ref/threephasedynamicload.html?s_tid=srchtitle_three%5C%20phase%5C%20dynamic%5C%20load_1` (visited on 09/26/2022).

[47] "Grid code modification report GC0137: Annex 18-Enstore updated guide for GB grid forming converters V005," National Grid Code, 2021.

[48] "Rate of change of frequency (RoCoF) withstand capability," ENTSO-E, 2018.

[49] "AXAL-TT PRO 6/10(12) kV Mellanspänningskabel med PEX-isolering Medium Voltage Cables with XLPE Insulation."